SMHI

No 96, May 2001

Reports Meteorology and Climatology

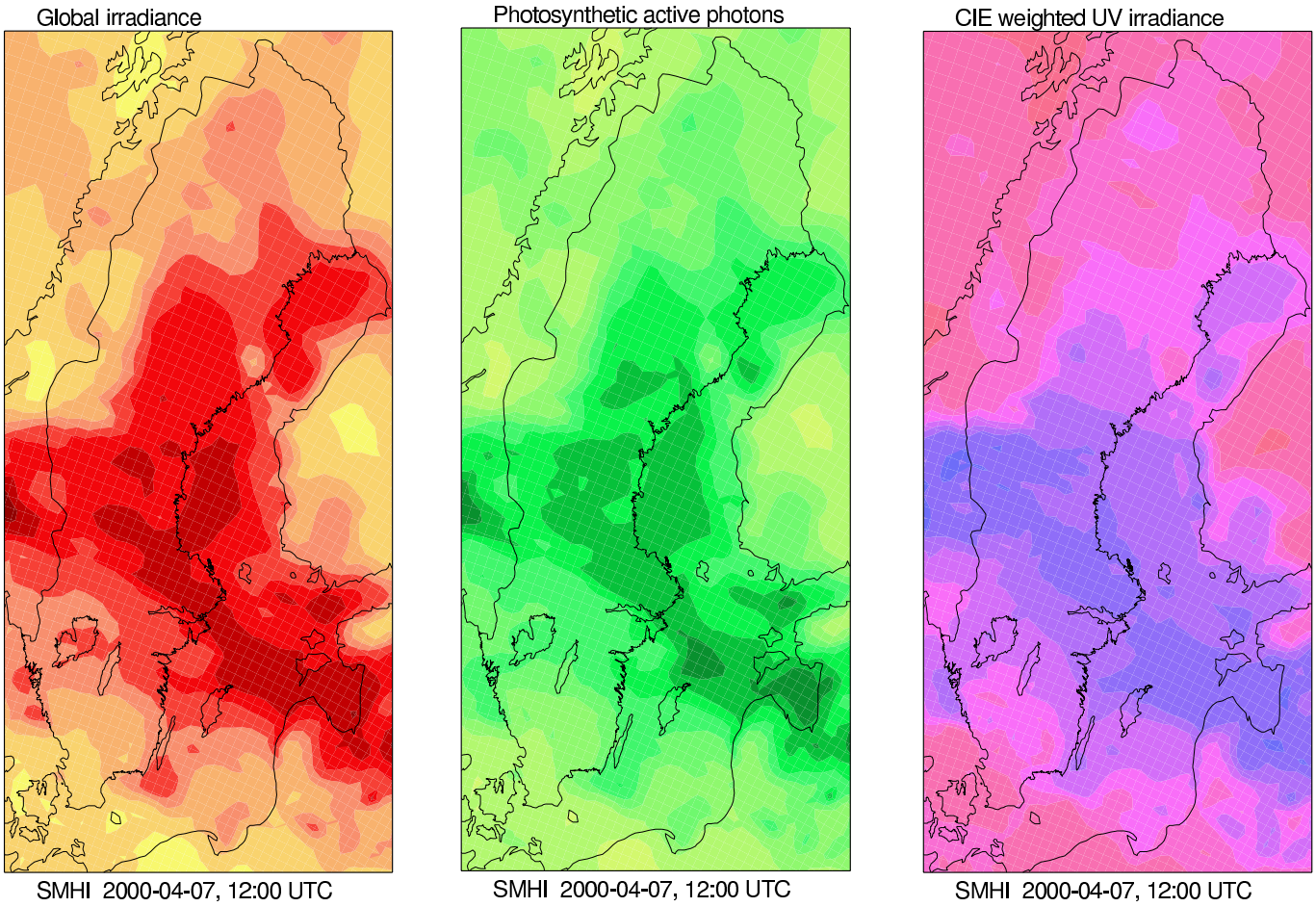

A system for modelling solar radiation parameters with mesoscale spatial resolution

Tomas Landelius
Weine Josefsson
Thomas Persson

RMK
No 96, May 2001

A system for modelling solar radiation parameters with mesoscale spatial resolution

Tomas Landelius
Weine Josefsson
Thomas Persson

Report Summary / Rapportsammanfattning

Issuing Agency/Utgivare	Report number/Publikation
Swedish Meteorological and Hydrological Institute S-601 76 NORRKÖPING Sweden	RMK No. 96
	Report date/Utgivningsdatum May 2001

Author (s)/Författare

Tomas Landelius, Weine Josefsson, Thomas Persson

Title (and Subtitle/Titel

A system for modelling solar radiation parameters with mesoscale spatial resolution

Abstract/Sammandrag

Today, modern analysis systems synthesise meteorological data from a number of sources, e.g.\ ground based SYNOP, satellites, radar, etc., into field information which enable us to model radiation at the Earth's surface on the mesoscale. At the Swedish Meteorological and Hydrological Institute (SMHI) we have set up a model system that produce hourly information in terms of field data with a resolution of about 22×22 km^2 for a geographic area covering Scandinavia and the run off region of the Baltic sea.

Presently, the model calculates fields of global-, photosynthetically active- (PAR), UV- and direct radiation based on output from a mesoscale analysis system, a high resolution limited area numerical weather prediction model (NWP), an ice model for the Baltic sea together with satellite measurements of total ozone. A spectral clear sky model lies at the heart of the model system. Its output is multiplied by a function which captures the influence of clouds and precipitation. Different cloud effect functions are applied to the different radiation components, with the exception of global- and PAR for which the same relation is assumed.

Measurements from the radiation network of SMHI were used for estimation and validation purposes. A first evaluation of the model system suggests that the RMSE for hourly global radiation data is on the order of 28% and about 16% for daily values. These errors are comparable to those obtained for models purely based on synoptic observations (SYNOP) (29% and 13%) . For UV radiation the figures are similar but for the direct radiation component they are worse; 53% and 31% respectively compared to 25% and 15% for the SYNOP models. To some extent the larger errors for the direct component could be explained by its sensitivity to scale differences when model grid squares are validated against point measurements.

Key words/sök-, nyckelord

modelling, solar irradiance, global radiation, photosynthetically active radiation, PAR, direct radiation, PAR, ultraviolet radiation, UV, CIE, erythema, sunshine duration, cloud transmittance

Supplementary notes/Tillägg	Number of pages/Antal sidor	Language/Språk
	52	English

ISSN and title/ISSN och titel

0347-2116 SMHI Reports Meteorology Climatology

Report available from/Rapporten kan köpas från:

SMHI
S-601 76 NORRKÖPING
Sweden

Contents

1 Introduction

The goal of the project ”Areal radiation”, funded by the Swedish Environment Agency, the Swedish Meteorological and Hydrological Institute and the Swedish Radiation Protection Institute, was to build a system that could produce fields of spatially distributed radiation quantities. Today the model system produces hourly information on global radiation, photosynthetically active radiation (PAR) and UV radiation on a horizontal surface at the ground level. The global radiation is actually calculated as the sum of direct and diffuse component. Therefore, also these components are available as well as the sunshine duration. For those not familiar with the radiation quantities a short presentation is given in the following sections. There is also a brief compilation of terms and abbreviations before the references at the end of the document. In the future it would be of great interest to complement the model with information about long-wave radiation and the reflected short-wave component, which are now the missing components in the radiation balance. The intention is that users should be able to extract all the radiation quantities from the mesoscale database as field data or as time series.

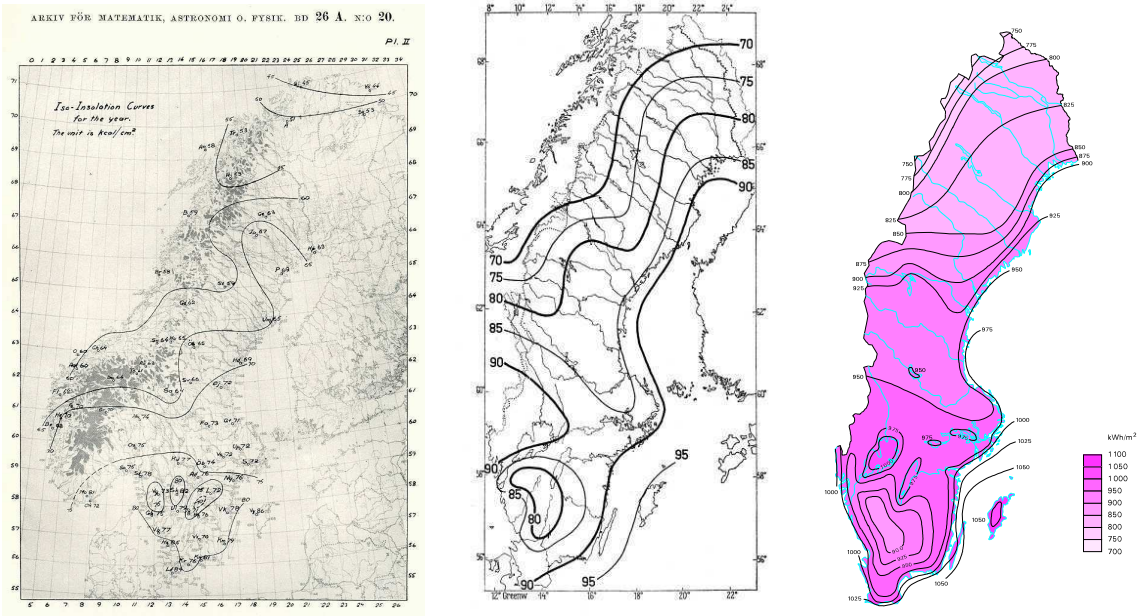

Figure 1: Global radiation climatologies. Left: T. E. Aurén (Aurén, 1939). Middle: C. C. Wallén (Wallén, 1966). Right: Swedish national atlas (SNA, 1995).

1.1 Background

At the beginning of the project in 1998, the above radiation quantities were either measured only at a few sites in Sweden or not measured at all. Models were employed to fill in gaps in the measurement series or to produce data for specific sites where input data were available. The aim of the proposed model system is to provide data with a spatial coverage and a resolution that was previously unreachable. Data should be fairly consistent and after validation against available measurements the quality will be known. Figure 1 shows some examples of earlier maps of global radiation. These have all been drawn manually based on measurements from sparse radiation networks.

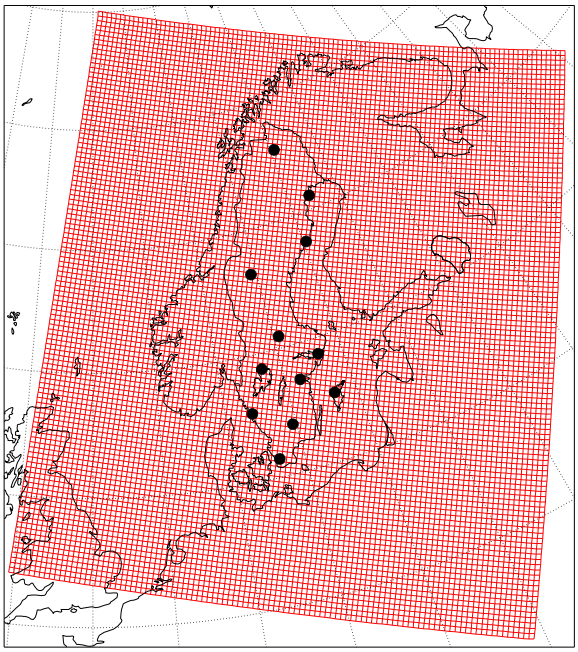

Figure 2: The model area covers Scandinavia and the Baltic with an approximate resolution of 22×22 *km*^{2}*. Stations in the current (1983–) SMHI radiation network are indicated with dots.*

There is a need for knowing the distribution of solar radiation with higher spatial resolution than what has previously been available. At the moment time series from twelve sites are available with information about direct solar radiation and global radiation, Figure 2. At a few sites also the downward long-wave radiation is measured. Except for the long-wave radiation measurements, these data are of high quality and are useful for many applications, in particular for studies where time series are of interest and for long term climate monitoring. However, data from the network is only representative for the limited area around the sites and the density of the network is sparse. There are also applications where the spatial distribution in combination with high temporal resolution is of interest. One example could be to determine where, within a certain region, to locate a solar cell system in order to optimise its production during the winter season.

Using the available network of twelve stations the spatial distribution of the radiation quantities could be described fairly well on land for Sweden on a monthly basis. The new system is expected to give a similar quality on a daily basis over a much wider area, Figure 2. However, there are regions in the field of interest, covering Scandinavia and the run off region of the Baltic sea, where the computed radiation fields will be less representative due to limitations in data used for model estimation. Typical examples are the mountainous areas in the northwest and the large open areas over the Baltic.

1.2 Data sources

The input and output fields that are produced by the system are adapted to fit the mesoscale analysis system at SMHI called MESAN, (Häggmark et al., 2000). This system covers the geographic region shown in Figure 2 with a grid of size 102×116 squares, corresponding to an approximate resolution of 22×22 km^2. Some of the input data to the radiation model system are retrieved directly from MESAN but there are other sources as well. The following is a list of all the input data providers:

- MESAN (Mesoscale analysis system)
- HIRLAM (High resolution limited area model)
- BOBA (Bohai and Balitc sea ice model)
- TOMS (Total ozone mapping spectrometer)
- Radiation measurements

Most input data are available or modelled every hour but some are acquired on a daily basis or obtained from climatologies. Regardless of source, the data is resampled to the MESAN grid. Measurements from the radiation network are used for validation purposes. In this case model output fields are interpolated to the points where the radiation stations are located in order to facilitate a comparison.

1.3 Modelled radiation quantities

The output fields described in this section are those that are produced by the system at the moment. However, the system is flexible enough to allow the inclusion of other radiation quantities in the future.

1.3.1 Global radiation

One component of the Earth's energy balance is the global radiation (downwelling shortwave radiation) at the surface, which among other things strongly affects the evaporation and evapotranspiration. The sum of the direct (beam), E_b, and diffuse solar radiation, E_d, (both considered within the spectral interval 280–4,000 nm) incident on a given planar surface from a solid angle of 2π steradians is called global irradiance, E_g. If nothing else is stated, the plane should be horizontal which is the case in this report.

$$E_g = E_b \cos Z + E_d. \tag{1}$$

The angle of incidence of the direct (beam) component equals the solar zenith angle, Z, for a horizontal surface. Knowing two components and using the relation in equation (1) the third component can be determined. Global radiation may be measured by a pyranometer. If a small disk shades such an instrument for the direct solar radiation it will measure the diffuse solar radiation. The output (voltage) from the pyranometer is proportional to the irradiance (unit W/m^2). It may be integrated over various time intervals to give the irradiation or the global radiation for an hour, a day or a month. In this report we use Wh/m^2 as the unit for irradiation.

1.3.2 Direct solar radiation

The solar radiation received from a solid angle subtended by the solar disk, on a plane perpendicular to the axis of this solid angle, is called direct solar radiation, E_b. It is synonymous with beam radiation. Radiometers for this parameter are called pyrheliometers and continuous monitoring of the direct solar irradiance requires a suntracker to point the instrument at the Sun. Pyrheliometers normally have a field of view which is larger than the angle subtended by the solar disk, which is about 0.5°. Therefore, pyrheliometer measurements will include some diffuse irradiance as well. Usually, this additional irradiance is negligible compared with the direct irradiance.

1.3.3 Sunshine duration

The sunshine duration is defined as the period when the direct solar irradiance is larger than 120 W/m^2, according to Recommendation 10 (CIMO-VIII), e.g. (WMO, 1996). Pyrheliometers can be used to measure sunshine duration. Traditionally, so called heliographs or sunshine recorders have been used. Data from these instruments often form the longest available records of solar radiation. There are measurements that started as early as in the late nineteenth century. Sunshine duration is valuable not only because there exist long-term series of climatological interest but also because it is easy to understand for most people. It is often used in tourist information to emphasise the sunny conditions at a resort. In northern Europe the sunshine duration acts as a good indicator of how people experience both the weather and the climate.

1.3.4 Photosynthetically active radiation

Spatial information about the PAR quantity will be of interest for example when estimating the growth of agricultural products on land and algae blooming in the sea. The photosynthesis is driven by light and individual photons are acting in its chemical reactions. To be active the photons must have a certain energy, contained in a well-defined spectral interval. PAR is defined as radiation in the 400 to 700 nm waveband. To calculate PAR one simply integrates the spectral solar radiation, E_λ, from 400 to 700 nm:

$$E_{PAR} = \int_{400}^{700} E_\lambda \, d\lambda. \tag{2}$$

This is the energy that could be active in the photosynthesis. However, the model output follows the guidelines recommended in (CIE, 1993) and reports PAR for plants as the total photon exposure in the 400–700 nm wavelength band.

The energy of a specific photon of wavelength λ or frequency ν is given by:

$$e_\lambda = h\nu = hc/\lambda \tag{3}$$

where $h = 6.63 \cdot 10^{-34}$ Js and $c = 3.0 \cdot 10^8$ m/s. If, for a small spectral interval $d\lambda$, the radiant energy is E_λ, then the number of photons per wavelength unit at wavelength λ will be:

$$n_\lambda = \frac{E_\lambda}{e_\lambda} \, d\lambda. \tag{4}$$

Therefore, instead of the integrated irradiance, E_{PAR}, the number of photons in the 400–700 nm waveband incident per unit time on a unit surface is calculated. This is also known as the photosynthetic photon flux density (PPFD):

$$\text{PPFD} = \int_{400}^{700} \frac{\lambda}{Nhc} \, E_\lambda \, d\lambda \tag{5}$$

where Avogadro's number $N = 6.023 \cdot 10^{23}$ is used to convert a number of photons to a number of moles. Instantaneous measurements, made with a flat or hemispherical sensor, should be reported as PPFD in mol/m^2/s. Values referring to a flat surface integrated over time should be reported as the exposure of photosynthetically active photons (PAP) in mol/m^2, with the time interval included in the text or in parenthesis. Ex: mol/m^2 (day).

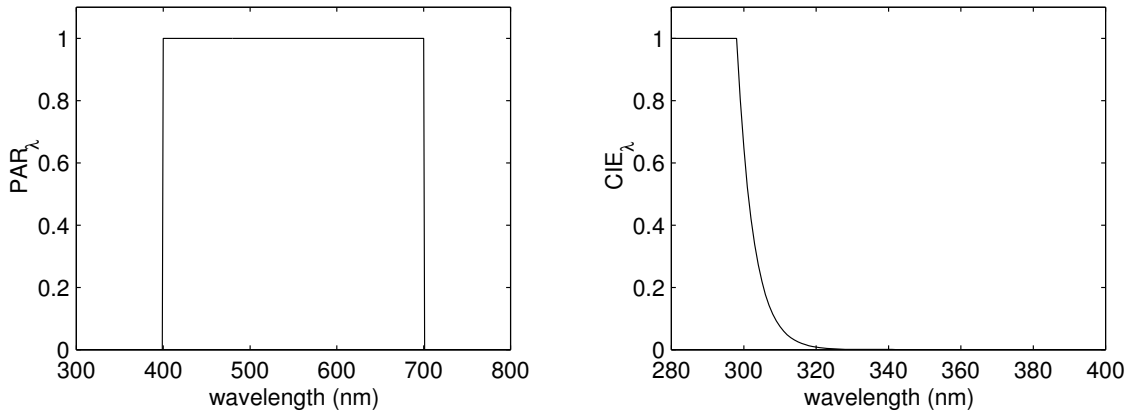

Figure 3: Left: Weight function for the photosynthetically active radiation. Right: Action spectra for erythema used in the calculation of the CIE weighted UV radiation.

1.3.5 CIE weighted UV radiation

The harmful influence of UV radiation on humans, flora and fauna is well known (WHO, 1994). Also materials such as paper, plastics and dyes are affected by UV which can cause objects of cultural and historical value to degrade in the long run.

The ultraviolet part of the spectrum is often divided into the UV-A (315–400 nm), UV-B (280–315 nm) and UV-C (200–280 nm) wavelength ranges. At the surface of the Earth there is no UV-C from the Sun. The cut-off in the solar spectrum due to atmospheric ozone and oxygen lies within the UV-B range. For many applications in biology, medicine and material sciences the effect of different wavelengths may vary considerable. Often, the damaging effect is large for the shortest wavelengths with a very rapid drop when moving towards the longer wavelengths. The efficiency a given wavelength has in causing a specific effect is given by its action spectrum, often normalised to unit efficiency at the wavelength causing maximum effect. These maxima are often located in to the short UV-B wavelengths and the efficiency in the UV-A is low. When it comes to the efficiency of UV to cause sunburn (erythema) there is an international agreement (ICNIRP, 1995) to use the so called CIE-action spectrum for erythema, (CIE, 1987). The wavelength dependence of this action spectrum is shown in Figure 3.

To calculate the erythemal effect one needs the spectral solar radiation E_λ, and the erythemal action spectrum CIE$_\lambda$. The cross correlation of the solar irradiance and the CIE-action spectrum yields the CIE weighted UV irradiance (CIE UV):

$$E_{CIE} = \int_\lambda E_\lambda \, \mathrm{CIE}_\lambda \, d\lambda. \tag{6}$$

Since most of the weight lies in the UV-B part of the spectrum, this parameter is more dependent on the amount of ozone than the global irradiance or the PAR are.

For public information the UV-index (no dimension) is used. The CIE UV, given in W/m^2, is converted into the corresponding UV-index by a multiplication with a factor of 40 m^2/W.

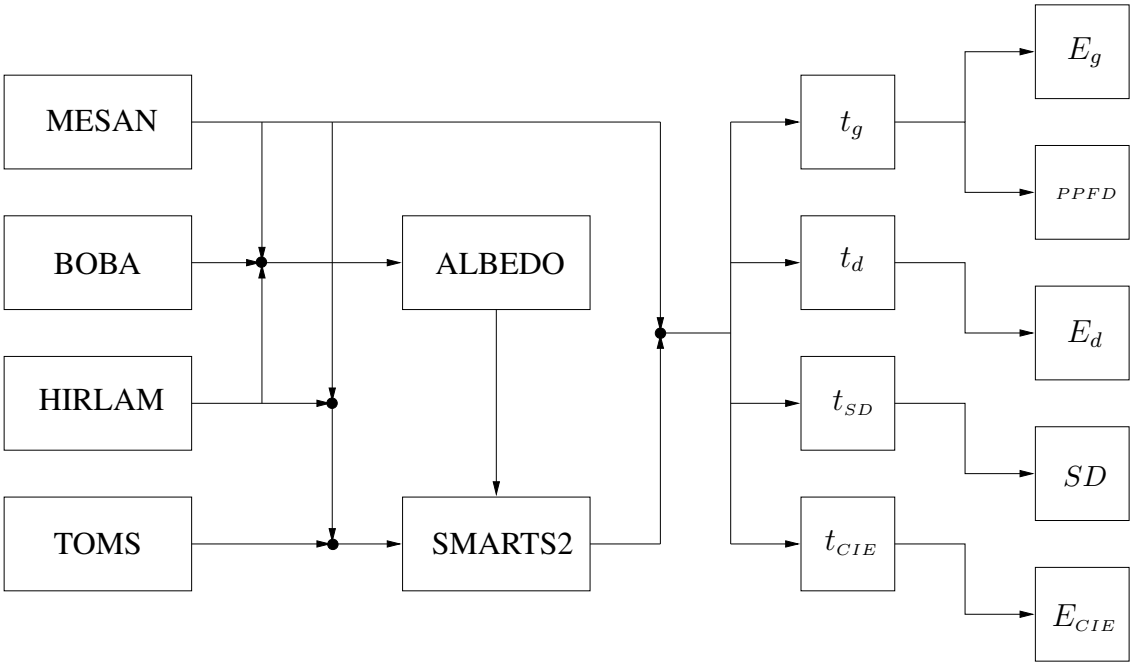

Figure 4: Schematic view of the model structure. Black dots indicate data flow junctions. The cloud effect functions are denoted with t *and an appropriate index.*

2 Model system

At the heart of the model system lies the clear sky radiation model. This model must be fed with appropriate input data from the sources given in section 1.2 to produce reliable results for the clear sky case. The clear sky output is then modified with respect to the clouds in order to arrive at the radiation quantities described in the previous section, see Figure 4. Below the clear sky model is introduced and motivated. The model structure is outlined and some operational aspects are discussed.

2.1 Radiation models

There exists a wide range of models from simple empirical ones up to advanced radiation transfer models. The latter may compute radiation spectrally line by line and through the atmosphere layer by layer. What model to chose is often determined by the availability of input data and depend on the operating conditions. Complex models need detailed input to produce accurate results. Our model system is supposed to produce hourly output fields in near real-time. Therefore, input data must be available with a sufficient spatial resolution on a daily basis.

Our choice between different models was mainly restricted by the lack of detailed aerosol and cloud data. Another limitation is the computational time. Each hour the radiation quantities should be determined in some ten thousand grid points. A lower limit may be based on demands for physical soundness, flexibility and quality. Soundness in this case means that important physical processes are explicitly parameterised. This allows us to test the effect of changing different input variables such as ozone or water vapour. The model should be flexible enough to permit new process parameterisations, e.g. concerning absorption and scattering. The quality of the model output must be sufficient both with

Table 1: Dynamic input parameters to SMARTS2

Albedo,	a (%)	Pressure,	p (hPa)
Altitude,	z (km)	Single scattering albedo,	ω
Asymmetry factor,	g	Solar zenith angle,	Z (deg)
Ozone column,	O_3 (atm-cm)	Ångström's turbidity coef.,	β
Precipitable water,	w (g/cm2)	Ångström's wavelength coef.,	α

respect to its spatial and temporal resolution.

We choose a hybrid solution. For the clear sky model we use a spectral radiation transfer code, with a number of parameterised physical process. The cloud effect functions, on the other hand, are parameterised using neural networks whose parameters are estimated from data. In the following sections the selected clear sky model is given a brief presentation.

The clear sky model we selected is SMARTS2 (Simple Model of the Atmospheric Radiative Transfer of Sunshine), (Gueymard, 1995). It was kindly made available to us by Christian Gueymard at the Florida Solar Energy Center in January 1998. SMARTS2 is a clear sky, two-stream, spectral model for the solar spectrum with one atmospheric layer. All scattering and absorption processes are explicitly parameterised.

We also considered using a separate model for the CIE UV. The most promising alternative was to use a parametersied version of UVSPEC which is a high resolution spectral model dedicated to the UV region (Kylling et al., 1995). However, with the input data we have available, it turned out that our parameterised version of UVSPEC and SMARTS2 gave almost identical results when modelling the CIE UV. In the light of this we decided not to use a special model in the UV region.

The spectral resolution of SMARTS2 is 1 nm in the interval 280–1,700 nm and 5 nm between 1,700 and 4,000 nm - 1,882 wavelength bands in all. The model has several input parameters and they are summarised in Table 1. For a detailed model description see the reference (Gueymard, 1995). One example of the output from SMARTS2 is shown at the top of Figure 5. The input parameters used to produce this output are: $p = 1,013$ hPa, $z = 0$ km, $O_3 = 0.334$ atm-cm, $w = 1.2$ g/cm^2, $\alpha = 1.3$, $\beta = 0.045$, $\omega = 0.90$, $g = 0.64$, $Z = 60^\circ$ and $a = a_\lambda$ (vegetation). Even though the internal computations in the model system are done spectrally, all output fields are in this application broadband quantities. However, the spectral property opens up for future model extensions.

Since land areas of size 22×22 km^2 are seldom homogeneous, the model system applies SMARTS2 to five subgrid areas with different spectral reflectances. The contribution of these subareas to the total output are controlled by their fraction of the grid area. This procedure is discussed in more detail in section 3.1. To get a feeling for the computational complexity of SMARTS2 it can be said that processing one field of size 102×116 (11,832 grid squares) with different albedo in order to get one output field takes about one minute on a Sun Ultra 1 (143 Mhz) workstation.

2.2 Operational aspects

The model system is intended to run almost in real-time. In practice, the delay will be about one day in order for all input data to be available. Producing fields for all five radiation quantities takes about 30 minutes on the workstation and most of this time is

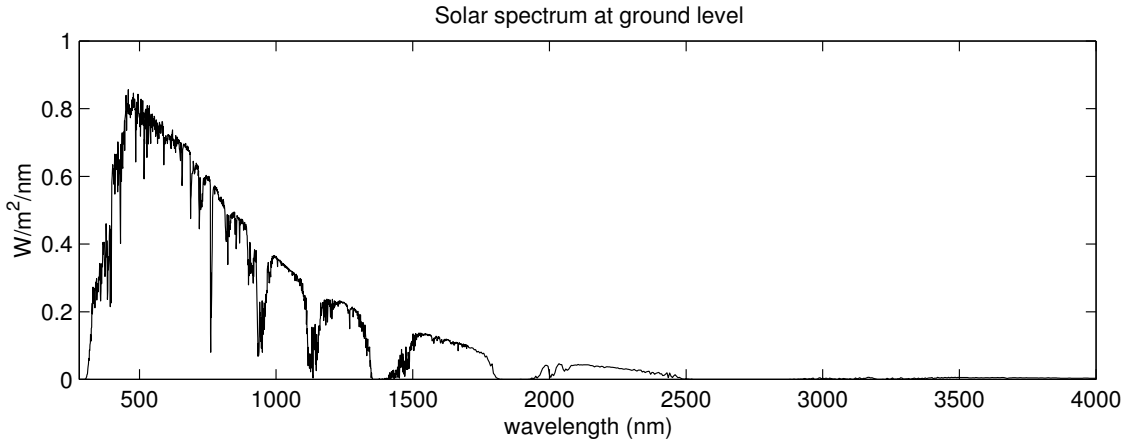

Figure 5: Clear sky solar irradiance spectrum modelled by SMARTS2. See text for details on input parameters.

spent running the SMARTS2 model. Tentative studies indicate that a reparameterisation of SMARTS2, using a neural net, would increase the RMSE from 28% to 30% (hourly global radiation) but the speed up gained would be of the order of 300 which would decrease the run time for the entire system to about one minute. In a reanalysis situation where decades of data must be processed such a reparameterisation would become necessary.

The run time reported above is only valid when all grid points need to be processed, i.e. when there are no "night" points. This means that the time it takes to produce a set of hourly radiation fields for one day will, in the mean, be shorter than 12 hours, leaving some time for a possible rerun in case of failure.

The system also has to be able to handle missing input data. This can be done in many ways but our approach is to rely on persistence in the first place and as a last resource use climatological values. This last climatological step is not implemented in the current system.

When HIRLAM data are required for model computations at time T the +06 to +11 forecasts valid at the actual hour T are used (a +06 forecast is only available for the hours 00, 06, 12 and 18 UTC). If such a forecast is unavailable, data is acquired in the following order: 1. The longer +12 to +17 forecasts valid at the actual hour T. 2. The +06 to +11 forecast valid for the previous hour $T - 1$. 3. The +06 to +11 forecast valid for the next hour $T + 1$.

MESAN data is requested as the analysis for the actual hour T. If this analysis is not available analyses valid at other hours are brought into use in this order: 1. At the previous hour $T - 1$. 2. At the next hour $T + 1$. 3. As the mean of the analyses at times $T + 02$ and $T - 02$.

When it comes to the BOBA model and the total ozone measurements, the data most recent in time is used. The BOBA model produce output fields every sixth hour while the ozone measurements are available on a daily basis.

3 Clear sky model

The model data sources were described in section 1.2. Some of these parameters can be used directly but most of them need to be processed before they can be input to the clear sky model as shown in Figure 4. The preprocessing of these input parameters is described

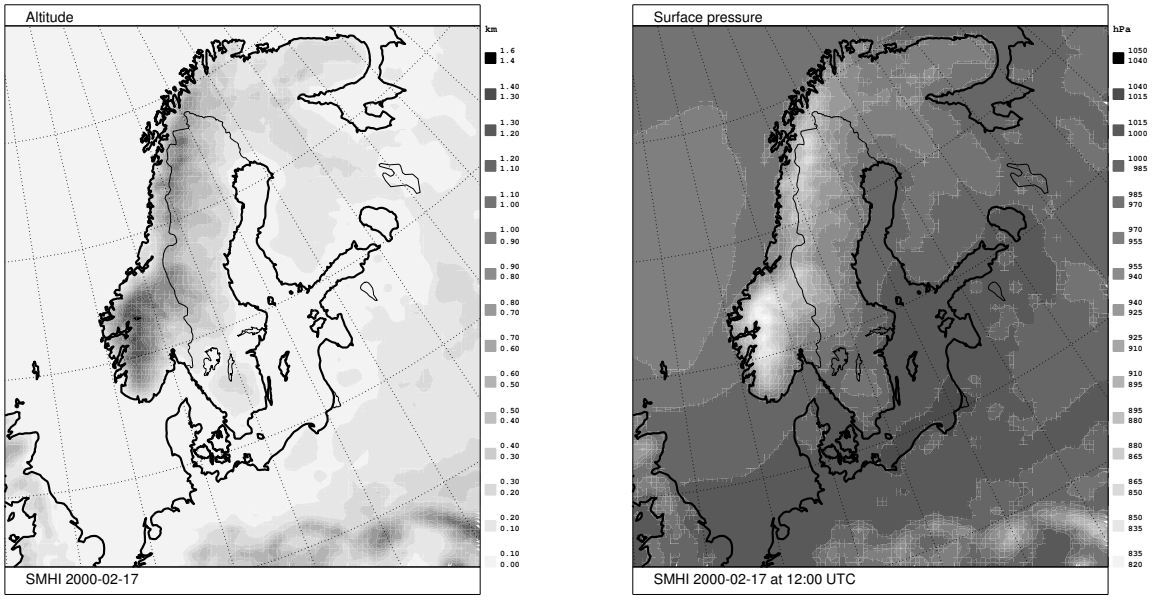

Figure 6: Left: Altitude field. Right: Example of a surface pressure field.

in this section which is ended with a presentation of some model output examples.

3.1 Input parameters

There are ten input parameters to SMARTS2, as indicated in Table 1. Common to all of them is that they must be adapted to the MESAN grid. The following subsections outlines how the different input parameters are obtained.

3.1.1 Altitude and surface pressure

The altitude and the surface pressure parameters are obtained from HIRLAM which like MESAN has a spatial resolution of 22×22 km^2. However, HIRLAM covers a larger area so the data corresponding to the MESAN grid points need to be extracted. Since the two grids overlap there is no need to resample the data from HIRLAM.

In 1871 Rayleigh discovered that air molecules scatter radiation and his findings lead to the explanation of the blue sky. Today, this effect is known as Rayleigh scattering and it is directly proportional to the surface pressure, describing the mass of the overlying atmosphere. Examples of altitude and surface pressure fields are shown in Figure 6.

3.1.2 Geographic position and solar zenith angle

Latitude and longitude values for all grid points are given by the MESAN geometry. The solar zenith angle is calculated from the latitude and longitude together with the time given as year, month, day and hour (minute value is zero). This makes the zenith angle correspond to the time at which the MESAN analysis and the HIRLAM forecast are valid. The computations are based on Kepler's equation and also accounts for the effect of refraction to produce the apparent solar zenith angle.

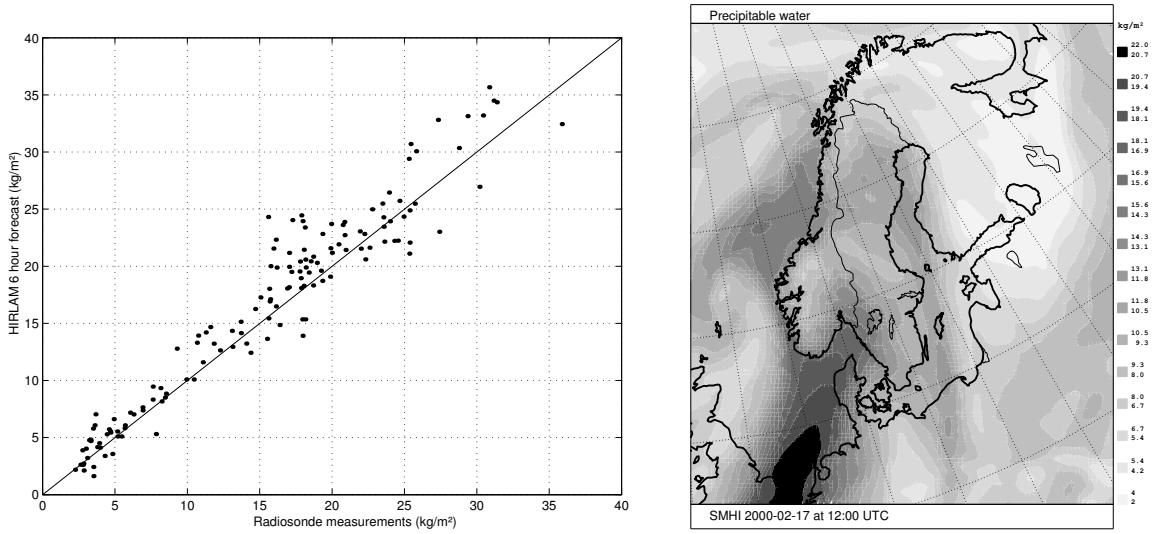

Figure 7: Left: Scatterplot showing the correlation between measured and modelled precipitable water. Right: Example of a precipitable water field.

3.1.3 Precipitable water

Absorption of solar radiation by water vapour is important, especially in the infrared (IR) and near infrared parts of the spectrum. In our model system this absorption is parameterised using the column precipitable water, which is the vertically integrated water vapour.

The traditional method for measuring the water vapour distribution in the atmosphere is to observe the relative humidity by a hygrometer or the dew point temperature using a wet thermometer along with the air-temperature itself. These measurements are connected with large uncertainties and most measurements are done at screen level, about 1–2 m above the ground. It is not believed that they should be highly representative for the total amount of water vapour in the atmosphere.

However, using balloons it is possible to get the vertical distribution of water vapour in the atmosphere. Balloon soundings are done regularly about twice a day at a limited number of stations. It has been the fundamental way to study the atmospheric water vapour since the 1930-ties. Due to the fact that the surface is both the source and sink for water in the atmosphere there is a rather good correlation between the ground level observations and the soundings. This is particularly true for longer time periods.

Presently several new sources of data are emerging. Sensors on board satellites measure the water vapour in the upper atmosphere and the integrated values may be obtained by studying the time delay in GPS signals. However, also numerical forecast models for the atmosphere, such as HIRLAM, include the water cycle. After some time the model, which is initialised by observations and some starting conditions, will spin up and produce fields of pressure and specific humidity that corresponds to a realistic water vapour field.

The input to the SMARTS2 model is the precipitable water which is the amount of condensed water obtained by vertical integration of the water vapour. It is often expressed in units like g/cm^2 or kg/m^2. Integrated water vapour fields, based on information about pressure and specific humidity from HIRLAM, have been compared with balloon soundings, Figure 7 (left). The errors are of about the same order as the inaccuracy of the observations. This means an RMS error of 17% and an MBE of some 7.3%. The advantage of using field data is that they already provide the spatial coverage. There is no need for interpolation from sparse data that would introduce additional uncertainties. An

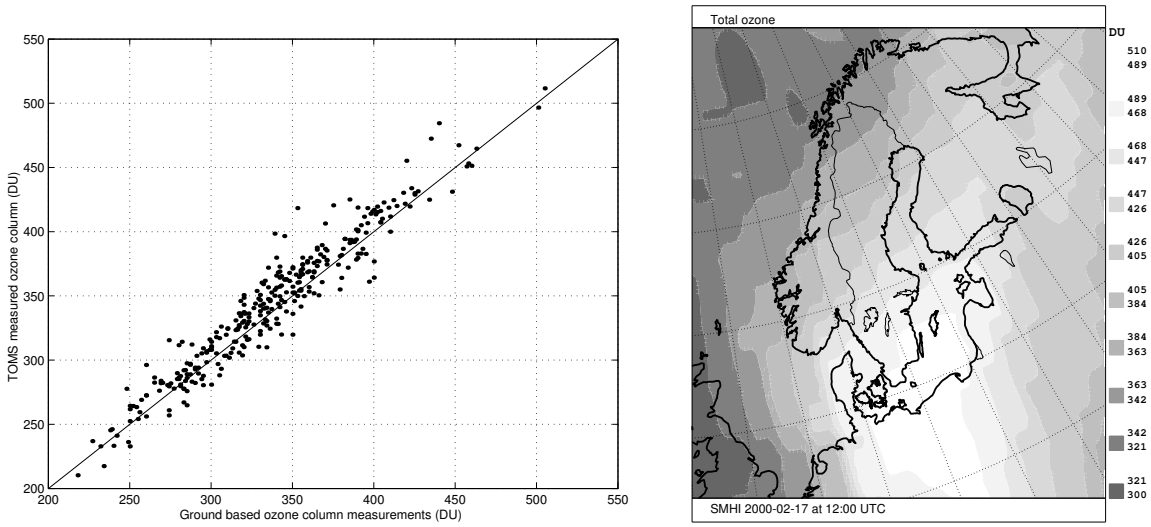

Figure 8: Left: Scatterplot showing total ozone (during 1998) measured from the ground at Norrköping (58.58° N) and the corresponding TOMS data interpolated to the same location. Right: Example of TOMS field with total ozone.

example with a precipitable water field is presented to the right in Figure 7.

3.1.4 Total ozone

Ozone absorbs solar radiation mostly in the UV and the visible part of the spectrum. There is also absorption and emission at longer wavelengths, not considered here. The efficiency of the absorption is slightly temperature dependent, but here temperature profiles from the US62 standard atmosphere is used (Anderson et al., 1986). Most of the atmospheric ozone, about 90% of the total amount, is maintained in the lower stratosphere. Therefore, a possible future improvement would be to let temperature values from a high level in HIRLAM control the ozone absorption.

Today it is not possible to regularly obtain the vertical distribution of ozone. However, knowledge about the spatial and temporal variation of the vertically integrated value, the total ozone column, should be good enough for this application. A future version of the NWP model at the European Center for Medium range Weather Forecasts (ECMWF) is said to include ozone which could then easily be resampled to the appropriate resolution and put into the model system.

There are a number of satellites observing this parameter. One of them, the Earth Probe, carries a TOMS (Total Ozone Mapping Spectrometer) instrument and data is available from the Internet in near real-time. A scatterplot illustrating the relation between between ground based measurements and the interpolated satellite data during 1998 is given in Figure 8. Some of the differences are due to to non-synchronisation, i.e. that measurements are recorded some hours apart. A more precise intercomparison reveal an RMSE of 3.0% and an MBE of 0.6% for the period 1996-07-17 to 2000-04-15 (Josefsson, 2000). An example of the total ozone field produced by the TOMS instrument is given to the right in the same figure.

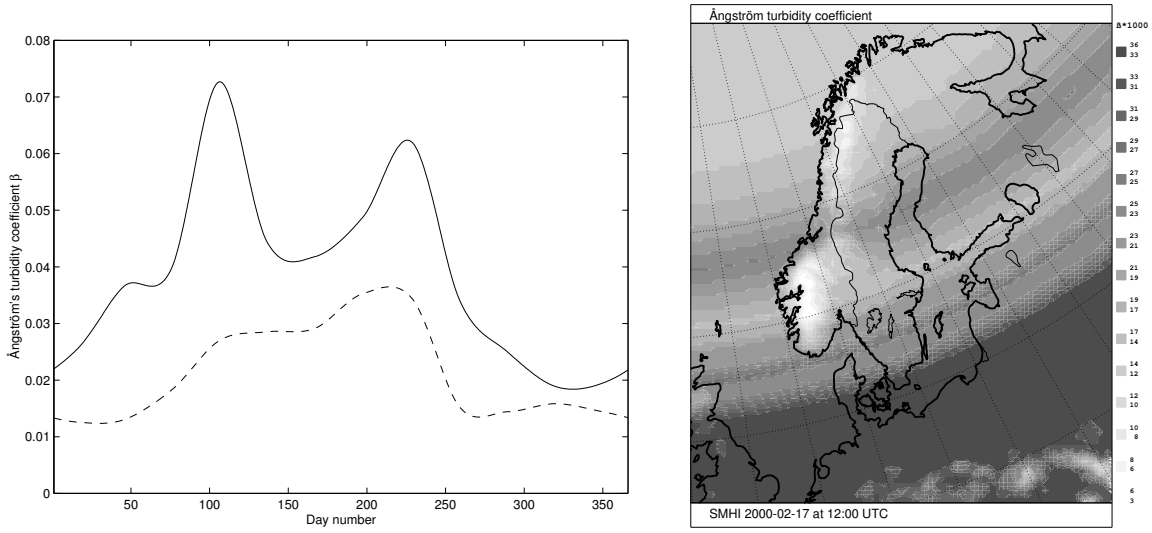

Figure 9: Climatological turbidity. Left: Daily values for β in Lund, $55.72°$ N (solid line) and Kiruna, $67.83°$ N (dashed line). Right: Field showing the geographical distribution of the turbidity coefficient for a given day.

3.1.5 Other atmospheric gases

There are several other gases in the atmosphere with absorption bands in the solar part of the spectrum, e.g. carbon dioxide, oxygen, nitrous dioxide and sulphur dioxide. These gases are included in the SMARTS2 model but for this application they can be treated as having a constant concentration. With the exception of NO_2 their amounts are obtained from the US62 standard atmosphere, (Gueymard, 1995). The total column of NO_2 is set to a typical summer value of $6.00 \cdot 10^{-4}$ instead of $2.04 \cdot 10^{-4}$ atm-cm which is used in the US62 atmosphere. The reason for this is that recent measurements points in this direction, (Pommeraux et al., 1997). The information concerning these atmospheric gases need only be improved if spectrally resolved data are of interest.

3.1.6 Aerosols

Among the inputs to the clear sky model, the aerosols probably presents the most challenging problem. Ångström (Ångström, 1929) proposed a power law as a model for the aerosol extinction effect at the Earth's surface given by $\tau_\lambda = \beta\lambda^{-\alpha}$, where α is known as the wavelength exponent and β as the turbidity coefficient. Indirect measurements of β are done at SMHI on a regular basis since 1977 (Persson, 1999). However, aerosols show a very complex behaviour. They act both as absorbers and scatterers and vary not only by their amount but also with respect to their size distribution, type (physical characteristics, chemical composition), and height distribution etc. As a consequence, the same α and β parameters may correspond to different combinations of these characteristics. In order to model the effects of aerosol scattering, the single scattering albedo ω and the asymmetry factor g also need to be parameterised.

The SMARTS2 model use the four parameters α, β, ω, and g to describe the aerosols but only the turbidity coefficient is allowed to vary. The other ones are set to the constant values $\alpha = 1.3$, $\omega = 0.90$, and $g = 0.64$ which approximately corresponds to a model by Shettle assuming a rural aerosol type, background aerosols above 2 km and a spring-summer profile (Shettle, 1989).

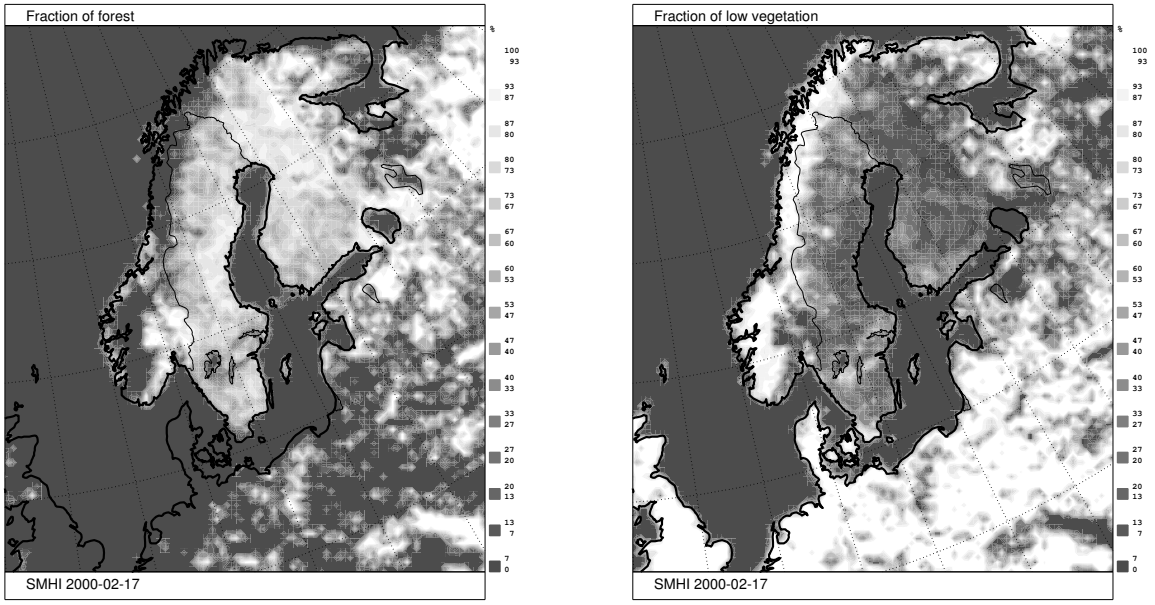

Figure 10: Fraction of forest (left) and low level vegetation (right).

At present there are no real-time estimates of the spatial distribution of the aerosol parameters. It is possible to obtain estimates of β from measurements of the direct solar radiation (Gueymard, 1998) and work is under way to incorporate such estimates, from the SMHI network, into the model system. Today, climatological values are used which are based on long-term averages of monthly median values from the twelve stations in the network. This climatology varies with the day of the year as well as the latitude and the altitude. The yearly variation varies from north (Kiruna) to south (Lund) as seen to the left in Figure 9. An example of a climatology field is shown to the right in the same figure.

3.1.7 Surface reflectance

The influence of ground reflectance on solar radiation is an important and complex issue. When it comes to radiation computations this parameter is closely connected to sky reflectance and consequently to the cloudiness. This aspect will be considered in the following paragraphs. Since the spectral irradiance under consideration lies in the region between 280 and 4,000 nm we need to parameterise the spectral reflectance for the same wavelengths. Further, calculations are made for grid squares which sizes are of about 400 km^2. Therefore, the spectral reflectances used in this model have to be representative for a scale of about 10–100 km^2. However, most available spectral reflectance data represents a certain surface or plant and may thus not be directly applicable. Another factor is that spatial homogeneity of the spectral reflectance may only be expected over sea and large woodlands.

Most land grid squares contain a mixture of surface types with disparate spectral reflectances. In the HIRLAM system there is information about the fractions of water, land with low vegetation and forest for each grid square, Figure10. The low vegetation category belong, within each grid square, to one of four subclasses: crop, short grass, tundra and bog/marsh. Note that these subclass names should not be taken literally. They are only meant to describe the most typical surface features. The geographical distribution of these subclasses are illustrated to the left in Figure 11. The real variation is large and too complex to be included in the system at the moment. For example, no urban surface class

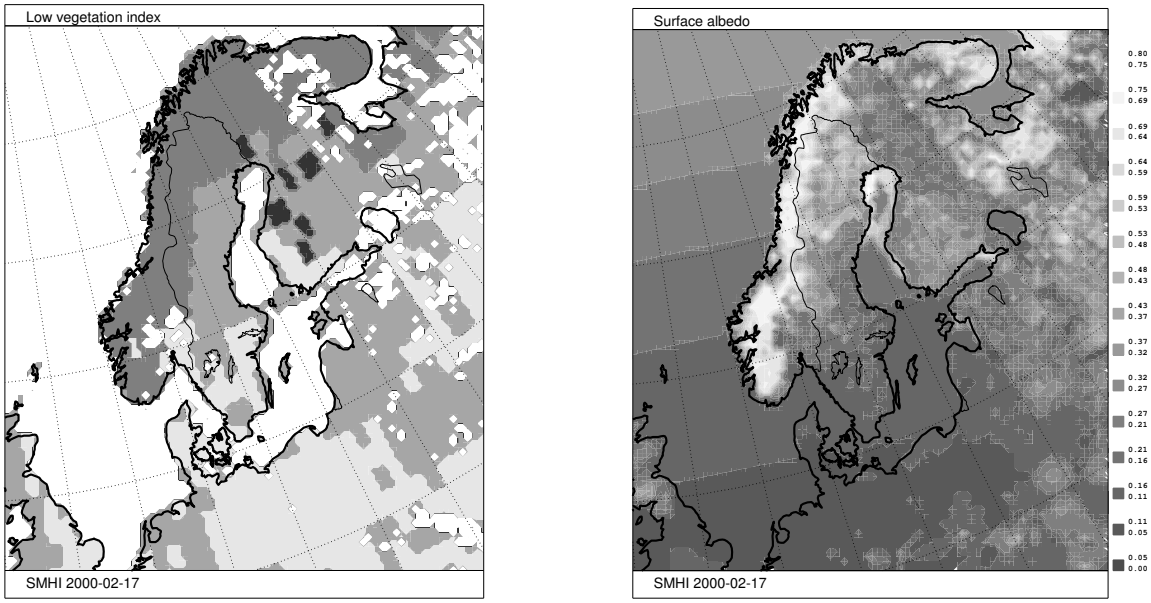

Figure 11: Left: Low vegetation, from white to dark : undefined, crop, short grass, tundra, and bog/marsh. Right: Example of modelled albedo for the global irradiance.

is included although there are a number of such areas within the modelled area.

The approach for the calculation of the surface reflectance is to extend the basic land use classes available in HIRLAM with two classes: ice and snow covered low vegetation. For each grid square, the fractions of these five classes are determined. Information about the ice concentration in the Baltic sea is available from the BOBA model. The fraction of forest is brought over from HIRLAM without modifications. HIRLAM also provides information about the snow depth which is used in the calculation of the fractions of bare and snow covered low vegetation.

During the season with snow cover a special snow category is introduced and the relative area covered by low vegetation is reduced. The fractional change depends on the snow depth and of the type of land use. The fraction of snow covered low vegetation is given by a product of the fraction of low vegetation (from HIRLAM) times a snow depth function $s(d)$ times a saturation value. This saturation value describes to what extent a deep snow cover will really cover the grid square. The saturation value is 0.8 for all subclasses except for the tundra for which it is 0.9. This means that there will always be a snow free fraction in a grid square with low vegetation.

The snow depth function is the same for all surfaces and is given by

$$s(d) = \begin{cases} \sqrt{d/12} & , \quad d \leq 12 \\ 1 & , \quad d > 12 \end{cases} \tag{7}$$

where d is the snow depth in centimeters. By subtracting the fraction of snow covered low vegetation from the fraction of total low vegetation, the fraction of bare low vegetation is obtained.

Each class is connected to an albedo in the UV range and a spectral reflectance based on data from literature (Bubier et al., 1997; Clark et al., 1993; Condit, 1971; Coulson and Reynolds, 1971; Asner, 1988; Asner et al., 2000; Grenfell et al., 1994; Gueymard, 1995; Hummel and Reck, 1979; Miller et al., 1997; Perovich, 1996; WMO, 1986). Depending on the state of the ground this albedo / reflectance is changed to deal with snow on ice and

Table 2: Land use classes in HIRLAM and in the reflectance calculations.

Basic classes	Extended classes	Reflectance type
Sea / lake	Sea / lake	Water
	Ice	Snow
Forest	Forest	Snow & veg
Low veg	Bare low veg	Vegetation
	Snow covered veg	Snow

forests, surface moisture, and the temporal aspects of different types of precipitation. The land use classes and their corresponding reflectance spectra are given in Table 2. These are all crude approximations but a precise description of the wavelength and bi-directional dependence of the reflectance in a specific grid square is not possible.

The clear sky irradiance is calculated as a linear combination of the irradiances $E_{\lambda,i}$, on the five different surfaces. The weights are given by the relative fraction f_i, occupied by each surface in the grid square, $i = \{$sea, ice, low vegetation, snow, forest$\}$:

$$E_\lambda = \sum_i f_i \, E_{\lambda,i} \left(a_i \, \frac{r_i^0(\lambda)}{a_i^0} \right). \tag{8}$$

Note that the reflectance $r_i^0(\lambda)$ spectrum in equation (8) is normalised with its nominal albedo a_i^0 and scaled to correspond to the dynamic albedo value a_i, that will be discussed below. Some constant nominal albedo values are given in Table 3. For water and forest areas the nominal albedo value is not constant but depends on the solar zenith angle and the snow cover respectively.

Sea / lake The water (sea / lake) albedo varies (increases exponentially) with the solar zenith angle. This dependence is parameterised in the SMARTS2 code and no extra input is needed.

Snow The reflectance for a snow covered surface varies considerable with age, temperature (melting/freezing) and depth. In and around larger cities snow-clearance and particle contamination affect the albedo during the winter. Although important, these effects are not considered explicitly in the model.

A dynamic function is used to determine if there has fallen enough snow during the past hours to build up a considerable cover of fresh snow:

$$y_{t+1} = \min\{1 \, , \, \alpha \, f(p_t) + (1 - \alpha) \, y_t\}. \tag{9}$$

Here, y is not the snow depth but a help variable used when establishing the fresh snow flag. When y gets above a threshold M the snow is considered fresh and the flag is set. It

Table 3: Nominal albedo values used in the irradiance calculations.

Irradiance	Fresh snow	Ice	Vegetation
Global / PAR	0.799	0.478	0.182
CIE UV	0.990	0.595	0.028

Table 4: Time constants (hours) and saturated snow albedo for different air temperatures in the calculation of dynamic snow albedos for PAR and global radiation (UV in parenthesis).

Temperature	Time constant	Saturated albedo
$T < -15°$	16 h	0.72 (0.89)
$-15° \leq T < -5°$	8 h	0.72 (0.89)
$-5° \leq T < 0°$	4 h	0.72 (0.89)
$0° \leq T < 5°$	2 h	0.64 (0.79)
$5° \leq T$	0.5 h	0.48 (0.60)

remains fresh until y falls below a lower threshold m (0.1), and the flag is unset. Before the snow is considered fresh next time, the help variable y must again get above the higher threshold M (0.99).

The constant α and the precipitation function $f(p)$, where p is the 1h accumulated precipitation, are chosen according to the following two criteria: It has to fall at least $2/n$ cm of snow per hour during n hours to create a layer of fresh snow. It takes 24 hours for a fresh snow layer to degrade into a non-fresh one. One choice that fulfills these two requirements is:

$$\alpha = 1 - m^{1/24} \tag{10}$$

$$f(p) = \frac{p}{2/n} \cdot \frac{M}{1-(1-\alpha)^{2/p}}. \tag{11}$$

Besides the flag, indicating a fresh snow cover, there is another function that explicitly calculates the snow albedo:

$$a_{t+1} = \begin{cases} a_t + \gamma(T)\,(a_s - a_t) & , \text{ no fresh snow} \\ a^0_{snw} & , \text{ fresh snow} \end{cases} \tag{12}$$

In the presence of newly fallen snow the snow albedo is set to that of fresh snow a^0_{snw}, see Table 3. The function γ is temperature (T) dependent and effects both how long it takes (t_c) for a fresh snow cover to degrade to a certain albedo value and what this albedo value eventually will be (a_s). These time constants and saturation levels are shown in Table 4. The output of $\gamma(T)$ results in that the relative distance between the dynamic albedo a_t and the saturated value a_s becomes less then ϵ (0.1%) after t_c hours:

$$\gamma(T) = 1 - \left| \frac{\epsilon\, a_s(T)}{a^0_{snw} - a_s(T)} \right|^{1/t_c}. \tag{13}$$

Ice The ice albedo is given as a linear combination between the nominal value in Table 3 and the actual snow albedo, where the snow function in equation (7) determine the influence of the snow cover:

$$a_{ice} = s(d)\; a^0_{snw} + (1 - s(d))\; a^0_{ice}. \tag{14}$$

Since information about the snow depth is only available for the land classes, an interpolated snow field for the ice covered water regions is produced based on the snow depth on the surrounding land areas.

Low vegetation Also the low vegetation albedo is based on a nominal value from Table 3. The dynamic albedo is found by a scaling of the nominal vegetation albedo. Different weights are used for the four subclasses with bare low vegetation subclasses depending on the status of the surface, Table 5. All subclasses share the same spectral reflectance function. Using the same standard reflectance for all types of vegetated surfaces may sound like an unnecessary simplification. However, since a grid square represents a large area and there is no representative data on spectral surface reflectances, we decided to use one and the same for all kinds of vegetation. In the same way as the snow albedo was affected by a flag indicating fresh snow, the low vegetation albedo is also dependent on whether or not the ground is to be considered wet.

The same function that is employed to calculate the fresh snow flag is used to calculate a flag indicating a wet ground. However, here the input is precipitation in terms of rain instead of snow. The effect of a wet ground can be seen in the right column of Table 5 where the wet values are obtained by reducing the vegetation albedo from Table 2 by 55%.

Forest Forest areas are treated in a special way. There is no class for snow covered forests. Instead the spectral forest reflectance is produced as a linear combination between the vegetation reflectance and the snow reflectance:

$$r(\lambda)^0_{fst} = w\, r(\lambda)_{snw} + (1-w)\, r(\lambda)_{veg} \tag{15}$$

$$w = \begin{cases} 0.2\, s(d) & , \text{ no fresh snow} \\ 1.0 & , \text{ fresh snow.} \end{cases} \tag{16}$$

In case there is a fresh snow cover, the nominal forest reflectance spectrum equals that of fresh snow ($w = 1$). When the snow is not considered to be fresh, 80% of the forest is seen as vegetation even if the snow cover is considered thick ($w = 0.2$, $s(d) = 1$, no fresh snow).

The actual reflectance spectrum is given by the nominal reflectance in equation (15) times the ratio between the dynamic forest albedo and the nominal forest albedo according to equation (17). These albedo values are both calculated more or less as linear combinations:

$$a^0_{fst} = w\, a_{snw} + (1-w)\, a_{veg} \tag{17}$$

$$a_{fst} = \begin{cases} s(d)\, 0.2\, a_{snw} + (1-s(d))\, 0.5\, a_{veg} & , \text{ no fresh snow} \\ 0.5\, a_{snw} & , \text{ fresh snow.} \end{cases} \tag{18}$$

Table 5: Albedo values assigned to dry and wet low vegetation subclasses for PAR and global radiation (UV values in parenthesis).

subclass	Dry	Wet
Crop	0.15 (0.023)	0.10 (0.016)
Short grass	0.15 (0.023)	0.10 (0.016)
Tundra	0.13 (0.020)	0.10 (0.016)
Bog / Marsh	0.13 (0.020)	0.10 (0.016)

Table 6: Static and dynamic input parameters to the surface reflection calculations.

Static	Dynamic
Fraction of low veg	2m temperature
Low veg index	Snow depth
Fraction of water	Ice concentration
Fraction of forest	1h acc precipitation
	1h acc snow

Here the weight w is given by the same expression as in equation (16). The only difference between the calculation of the nominal forest albedo in equation (18) and the nominal reflectance spectrum in equation (15) is that the snow and vegetation reflectance spectra are replaced by their corresponding albedo values. However, the expression for the dynamic forest albedo in equation (18) is more complex.

In the presence of a fresh snow cover, this albedo is set to 50% of the nominal albedo for fresh snow. The reason for this is that canopies shadow the ground making the snow look darker if it falls on a forested area than on an area with low vegetation. In the absence of fresh snow, the albedo is again given by a linear combination controlled by the snow cover function $s(d)$. Here the lower bound is given by 50% of the actual vegetation albedo ($d = 0$, $s(d) = 0$) and the upper bound by 20% of the actual snow albedo ($d > 12$, $s(d) = 1$). Again, the reason for reducing the nominal values is the effect of shadowing.

To conclude the discussion on reflectance calculations, a list of the input parameters used in these calculations is presented in Table 6. The low vegetation index is a field that for each grid square states which of the low vegetation subclass that is valid within the square, Figure 11 (left). An example that shows what a modelled global radiation albedo can look like is presented to the right in the same figure. Presently, available data found in the literature is too limited to make an objective albedo model. Several parameterisations in this model are subjective and ad hoc. When the model has been in use for some time it should be validated against measurements and the parameterisation should be reconsidered as better data become available.

3.2 Clear sky model output

In this section the output from the clear sky model is discussed. Here the sky is considered as clear when the MESAN data indicate that less than 2.5% of the sky is covered with clouds. Examples of hourly output field data is presented for all four radiation quantities; global-, direct-, photosynthetically active-, and CIE UV radiation. Scatterplots showing the correlation between modelled and measured radiation are presented for all but the photosynthetic radiation since no measurements were available for this quantity.

In Figure 12 the three scatterplots are shown for the period April–September 1998. The measurements of global and direct radiation come from 11 of the 12 stations (Kiruna excluded due to malfunction) in the SMHI radiation network and the UV measurements come from the station in Norrköping.

A constant albedo of 0.20 has been used in all calculations since the albedo routine presented in the previous section has only recently become available. The main reasons behind the large scatter of the direct radiation values are probably scale differences, erroneous MESAN data and the lack of information about the aerosols. Since the clear

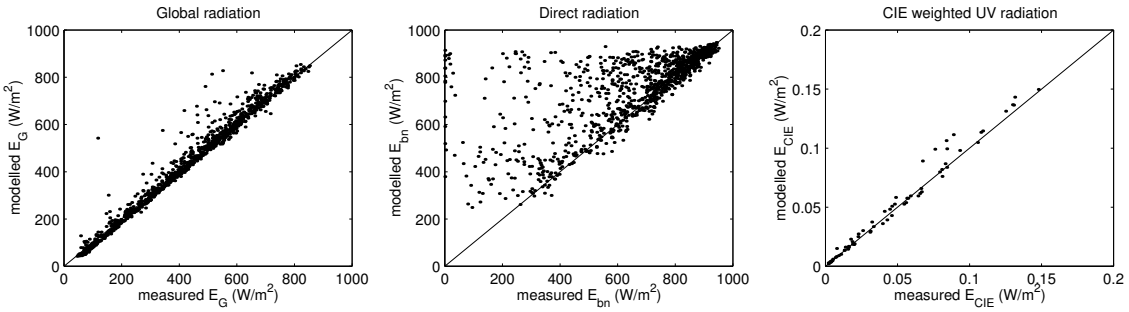

Figure 12: Scatterplot with hourly global- (left), direct- (middle) and CIE UV radiation for a clear sky during April–September 1998.

sky requirement on the cloud cover is based on a grid square of size 22×22 km^2 while the measurements refer to a single point it is possible that there are clouds at the station while the grid square is considered to be clear. The aerosol information is only based on climatological data and does not catch the natural variation which can be rather high.

Some error statistics for the clear sky models is presented in Table 7 where the problems in modelling the direct component becomes evident. Note that it should be possible to reduce the MBE (positive if the model overestimates) when the cloud effect function is introduced while the RMSE only is expected to become worse when the clouds are introduced.

The examples showing what the hourly clear sky field data can look like are taken from the date February 17, 2000 at 12 hours UTC (noon time in England). In Figure 13 fields with clear sky global-, photosynthetically active-, direct-, and UV radiation are given at the top left, top right, bottom left and bottom right respectively. An example with hourly output from the clear sky models for the date June 21, 1998 at Norrköping is shown in Figure 14. This can be seen as approximate upper bounds for the five different radiation quantities at this geographic location.

4 Cloud effect models

Besides the yearly and daily variation in the solar radiation that mainly depends on the solar elevation, clouds are the most important modulating factor in our latitudes. A large fraction of the radiation is reflected back into space from the cloud tops, some is absorbed and some transmitted. Clouds introduce a complexity in the radiation flow that will not always be possible to describe accurately by the one-dimensional models discussed here. For example, a sky with broken cloudiness has an uneven radiance distribution. Some

Table 7: Error statistics for the clear sky models (hourly values) during April–September 1998.

	Global	Direct	CIE UV
Samples	1,061	1,061	69
Correlation	0.99	0.69	0.99
MBE	2.4% (10 W/m^2)	15% (96 W/m^2)	0.72% (0.34 mW/m^2)
RMSE	8.9% (38 W/m^2)	29% (190 W/m^2)	11% (5.0 mW/m^2)

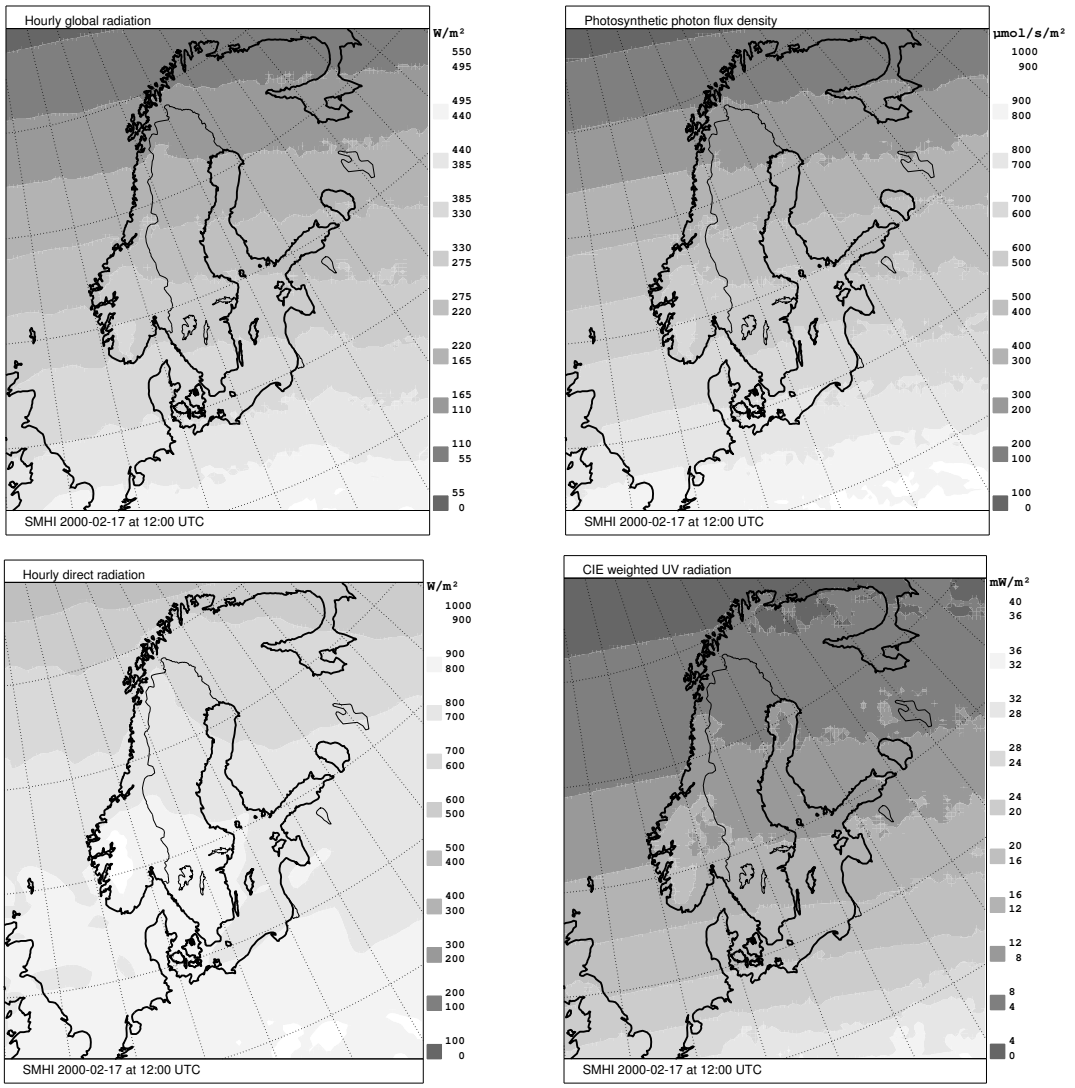

Figure 13: Hourly clear sky fields of global radiation (top left), PAR (top right), direct radiation (bottom left) and UV radiation (bottom right). All fields refer to the date February 17, 2000 at 12:00 UTC.

cloud sides are sunlit while others are in the shadow. The Sun itself may or may not be totally obscured, as seen from ground. This leads to considerable differences when modelling the surface irradiance. Clouds are also changing on spatio-temporal scales that cannot be resolved within this project.

The influence on radiation from clouds has to be parameterised on the mesoscale. With proper input data the radiation model can describe the radiation under clear skies which was shown in section 3.2. Therefore, the cloud parameterisation will be crucial for the quality of the model output fields. To accurately model radiation in cloudy regions of the Earth we need a proper and physically sound treatment of the cloud effect. The approach we suggest is to first model the clear sky irradiance and then adjust this value by multiplying it with a cloud effect function that takes as its input the solar zenith angle as well as the cloud and precipitation information available from MESAN.

Basically there are two effects that have to be considered. The most apparent one is the attenuation by the clouds that may be described by an effective cloud transmittance. This parameter varies considerably as a function of cloud amount and it also depends

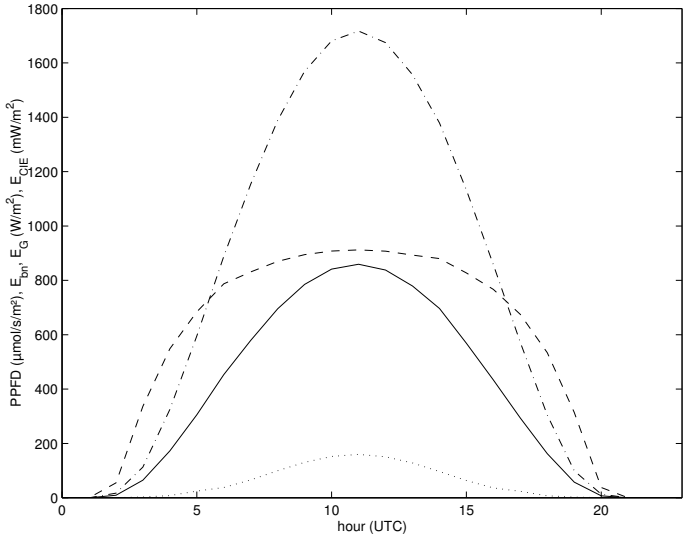

Figure 14: Examples of hourly output from the clear sky model for June 21 in Norrköping: PPFD (dash dotted line), direct irradiance (dashed line), global irradiance (solid line) and UV irradiance (dotted line). Note that the unit differs between the quantities.

on the cloud type. Another factor that will change is the multiple reflection between the ground and the atmosphere. The introduction of clouds will alter the multiple reflection fluxes compared to the clear sky case. The atmosphere will in this case have a different reflectance. There will also be a similar interaction between the top of the cloud layer and the overlying atmosphere. Therefore, the introduction of clouds into a one-layer model of the atmosphere calls for some special parameterisations in order to take care of the multiple reflection effects. A brief description of the utilised parameters and the parameterisation of the cloud effect is presented below.

4.1 Input parameters

Long periods with hourly information about clouds and their optical properties are seldom available for large regions. The MESAN system uses several data sources and its cloud information is a synthesis of data from both polar and geostationary satellites as well as ground based observations. The available data are given on the grid described in section 1.1. The temporal resolution is hourly for some parameters but normally the one hour resolution is obtained by interpolation of information that arrive every third hour. The available cloud parameters are listed in Table 8.

The cloud optical thickness varies considerably. Some of this variation is expected to be correlated to the difference between the cloud top and cloud base parameters. The cloud base parameter is only defined when there are clouds at the same height covering at

Table 8: Cloud related parameters available in MESAN.

Total cloud amount,	C_T (%)	Cloud top,	H_t (m)
Amount of low clouds,	C_L (%)	Cloud base,	H_b (m)
1h acc precipitation,	p_{1h} (mm)	Cloud base probability,	P_b (%)

least 3/8 of the celestial dome. Because of this, MESAN also outputs the probability for a significant cloud base. This parameter corresponds to the frequency of valid cloud base observations and can hence be used as a certainty measure for the cloud base parameter.

Very thick clouds tend to be connected with precipitation. The inclusion of precipitation information has proved to be a useful approach before, (Josefsson, 1989). In MESAN precipitation fields are available for various periods of integration. The quality of these fields is often low since the number of sources available in near real-time are few for this parameter. The number of automatic stations is low and data from the radar network sometimes introduces anomalous echoes that can erroneously be interpreted as precipitation. Despite these drawbacks, the cloud effect turned out to be better described when this parameter was introduced.

Besides the parameters given in Table 8 the solar zenith angle is used in the calculation of the cloud effect for the direct radiation and the sunshine duration. The reason for this is described in more detail in section 4.3. Also the albedo should be used as input to the cloud effect function. However, since the albedo model was developed in parallel with the rest of the model system, too few albedo data were available to be of any use when the first version of the cloud function was parameterised. The effect of neglecting the albedo in this model is commented on in section 4.4.

4.2 Cloud effect on global radiation, PAR and UV radiation

In this section we present a simple physical model and show that it can be seen as a special case of the more general cloud effect function we propose in section 4.5. The cloud effect used for PAR is the same as the one used for the global irradiance. The spectral distribution of the PAR lies in the middle of the solar spectrum and in many respects PAR is affected by the atmosphere in the same way as the global irradiance. The cloud effect function for the CIE UV has the same arguments as the one for PAR and global radiation but is otherwise a different parameterisation. One reason for this is the apparent relatively higher transmittance (about 30%) for the UV region which is due to the relatively larger multiple reflection components in the UV compared to the rest of the spectrum.

4.2.1 Clear sky

In the SMARTS2 model, two spectral components are computed: the direct beam, E_b and the diffuse solar radiation, E_d. The diffuse component is the sum of three components. They are the Rayleigh scattered, E_{dr}, the aerosol scattered, E_{da}, and the multiple reflected diffuse component, E_{dm}, see Figure 15. The global irradiance for a clear sky at a specific wavelength, E_g = $E_{g0\lambda}$, is the sum of these components, noting the influence of the zenith angle on the direct beam component:

$$E_{g0\lambda} = E_{b\lambda}\ \cos Z + E_{dr\lambda} + E_{da\lambda} + E_{0dm\lambda} \tag{19}$$

where the multiple reflected component in the SMARTS2 model is given by

$$E_{0dm\lambda} = \frac{\rho_{s\lambda}}{1 - \rho_{s\lambda}\rho_{d\lambda}}(\ \rho_{b\lambda}\ (E_{b\lambda}\ \cos Z) + \rho_{d\lambda}\ (E_{dr\lambda} + E_{da\lambda})). \tag{20}$$

Here $\rho_{b\lambda}$ is the spectral reflectance for the beam irradiance and $\rho_{d\lambda}$ is the spectral reflectance for the diffuse irradiance while $\rho_{s\lambda}$ is the spectral clear sky reflectance. The differentiation between $\rho_{b\lambda}$ and $\rho_{d\lambda}$ is made in SMARTS2 (Gueymard, 1995) to account

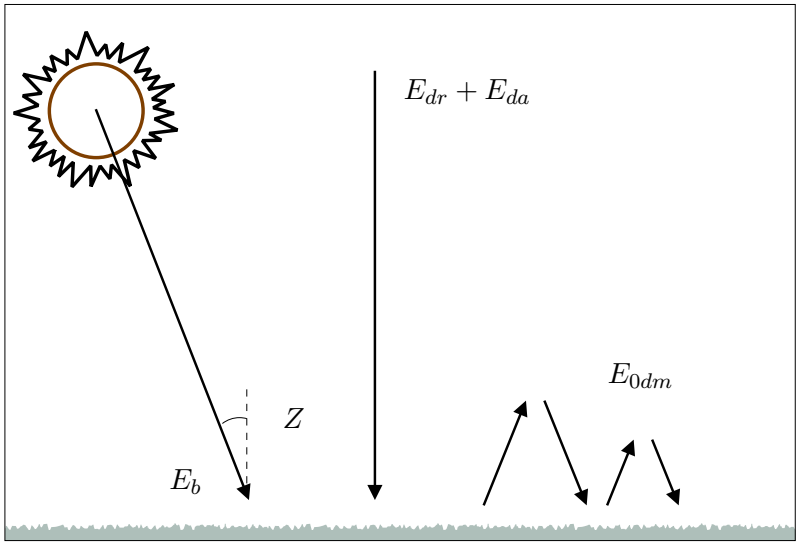

Figure 15: Schematic radiation components for clear sky.

for the non-Lambertian characteristics of natural surfaces. In our application the spatial scale is so large that there will be a complex mixture of different surfaces within each grid square. Therefore, this distinction will be impractical and both $\rho_{b\lambda}$ and $\rho_{d\lambda}$ may be approximated with $\rho_{g\lambda}$ which gives

$$E_{0dm\lambda} = \frac{\rho_{s\lambda}\rho_{g\lambda}}{1 - \rho_{s\lambda}\rho_{g\lambda}}(E_{b\lambda}\ \cos Z + E_{dr\lambda} + E_{da\lambda}) \tag{21}$$

and the cloud free component at the ground is hence given by

$$E_{g0\lambda} = \frac{1}{1 - \rho_{s\lambda}\rho_{g\lambda}}(E_{b\lambda}\ \cos Z + E_{dr\lambda} + E_{da\lambda}). \tag{22}$$

The following paragraphs will pinpoint some of the problems that occur when clouds are introduced.

4.2.2 Overcast sky

One simple cloudy case is that of one horizontally homogeneous cloud layer covering the whole sky, Figure 16. However, even in this idealised case several parameterisation problems arise. The clear sky model produces values valid at the surface level under cloud free conditions. In the overcast case radiation start interacting at the top level of the cloud, which could be several thousands of meters above the ground. From MESAN there is information about the altitude of the cloud top which in practice makes it possible to model the irradiance at this level, $E_{c\lambda}$, knowing the spectral reflectance of the cloud top. By applying an appropriate value for the cloud transmittance, the transmitted radiation, $E_{t\lambda}$, can be calculated. Below the cloud the multiple reflections have to be accounted for using accurate values for the sky reflectance (including the spectral cloud base reflectance) and the ground reflectance.

Let us assume that there is a single homogeneous cloud layer, which is so close to the ground that the effects due to height are negligible. At the cloud top the irradiance is then given by equation (22) with the cloud reflectance $\rho_{c\lambda}$ replacing the ground reflectance $\rho_{g\lambda}$:

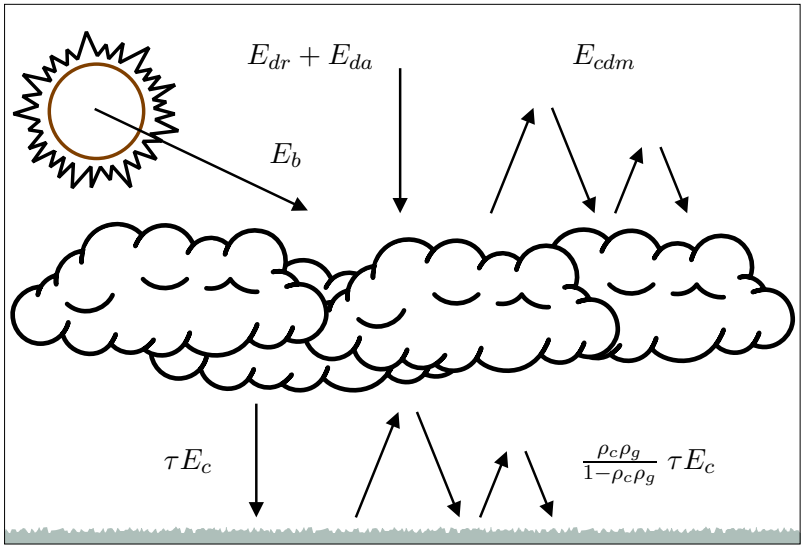

Figure 16: Schematic radiation components for cloudy skies. Simple case with one layer which is completely overcast.

$$\begin{aligned} E_{c\lambda} &= E_{b\lambda}\ \cos Z + E_{dr\lambda} + E_{da\lambda} + E_{cdm\lambda} \\ &= \frac{1}{1-\rho_{s\lambda}\rho_{c\lambda}}(E_{b\lambda}\ \cos Z + E_{dr\lambda} + E_{da\lambda}). \end{aligned} \tag{23}$$

Next, consider the conditions at the ground below the cloud cover. The effective transmittance of the clouds is assumed to be τ. Taking the additional multiple reflection below the cloud into account we arrive at an expression for the irradiance at the ground:

$$\begin{aligned} E_{gc\lambda} &= \tau\, \frac{1}{1-\rho_{c\lambda}\rho_{g\lambda}}\, E_{c\lambda} \\ &= \tau\, \frac{1}{(1-\rho_{s\lambda}\rho_{c\lambda})(1-\rho_{c\lambda}\rho_{g\lambda})}\, (E_{b\lambda}\ \cos Z + E_{dr\lambda} + E_{da\lambda}) \\ &= \tau\, \frac{1-\rho_{s\lambda}\rho_{g\lambda}}{(1-\rho_{s\lambda}\rho_{c\lambda})(1-\rho_{c\lambda}\rho_{g\lambda})}\, E_{g0\lambda}. \end{aligned} \tag{24}$$

Note that the cloud transmittance τ depends on the cloud type which we have knowledge about from the cloud top and base parameters together with the information about precipitation.

4.2.3 Broken cloud cover

In case of a sky with a broken cloud cover we simply divide the grid area into two parts, one completely overcast and another with clear sky. The cloud effects are assumed to occur only in the overcast part, Figure 17. The clear and cloudy irradiances, given by equations (22) and (24), are then linearly weighted according to the total cloud amount C_T:

$$E_{g\lambda} = (1 - C_T)\, E_{g0\lambda} + C_T\, E_{gc\lambda}$$

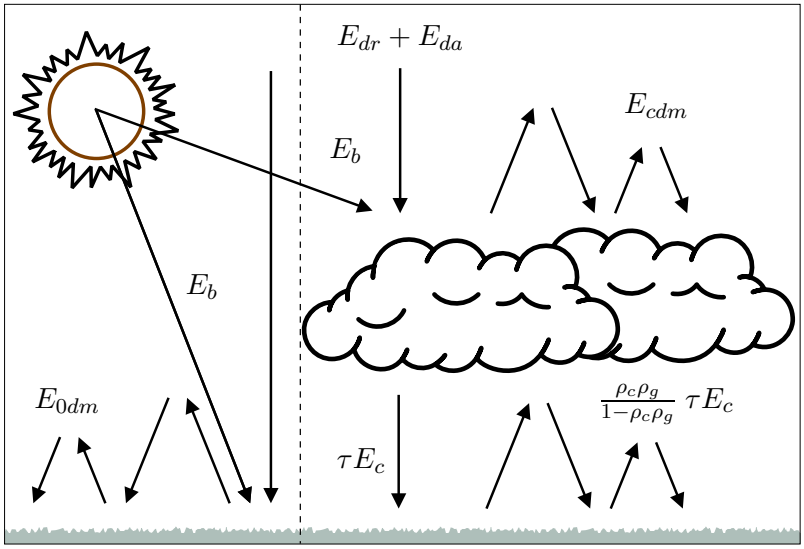

Figure 17: Schematic radiation components for a sky with broken cloud cover.

$$
\begin{aligned}
&= (1 - C_T)\, E_{g0\lambda} + C_T\, \tau\, \frac{1 - \rho_{s\lambda}\rho_{g\lambda}}{(1 - \rho_{s\lambda}\rho_{c\lambda})(1 - \rho_{c\lambda}\rho_{g\lambda})}\, E_{g0\lambda} \\
&= t_g(C_T, \rho_{c\lambda}, \rho_{g\lambda}, \rho_{s\lambda})\, E_{g0\lambda}. \qquad (25)
\end{aligned}
$$

From the discussion above it is clear that our approach, where the spectral global irradiance is given by the clear sky value times a function t_g, describing the cloud effect can represent a simple, yet physically sound, one-layered cloud model.

In real situations there may be several broken cloud layers at various heights. This will complicate the model but the the approach can still be summarised as finding a cloud effect function, which describes the effect that clouds and precipitation have on the clear sky irradiance. This function will in the general case also depend on the amount of low clouds, cloud top, cloud base, significance for the cloud base as well as the one hour accumulated precipitation.

4.3 Cloud effect on direct radiation and sunshine duration

Again we present a simple model to motivate the use of a cloud effect function in the calculation of the direct radiation and consequently also for the sunshine duration.

The direct solar irradiance $E_{b\lambda}$ is computed spectrally by SMARTS2 for the clear sky case. For this quantity the influence from ground and sky reflectances are negligible but the clouds have a large impact. Here we assume that all wavelengths are equally affected by the clouds and therefore restrict the discussion to the spectrally integrated value E_b.

The effect of optically dense clouds is very much putting the direct component on or off. However, thin clouds may attenuate the direct solar radiation in varying degrees. In particular, high clouds are translucent for the direct solar radiation. There are also clouds composed of smaller elements as altocumulus and stratocumulus. In between these elements there is a possibility for direct component to reach the ground.

However, low and middle level clouds often have a considerable vertical extension. Such clouds give rise to a screening effect on the direct solar radiation, sometimes called the coulisse effect. The effect disappears under overcast and cloud free conditions and

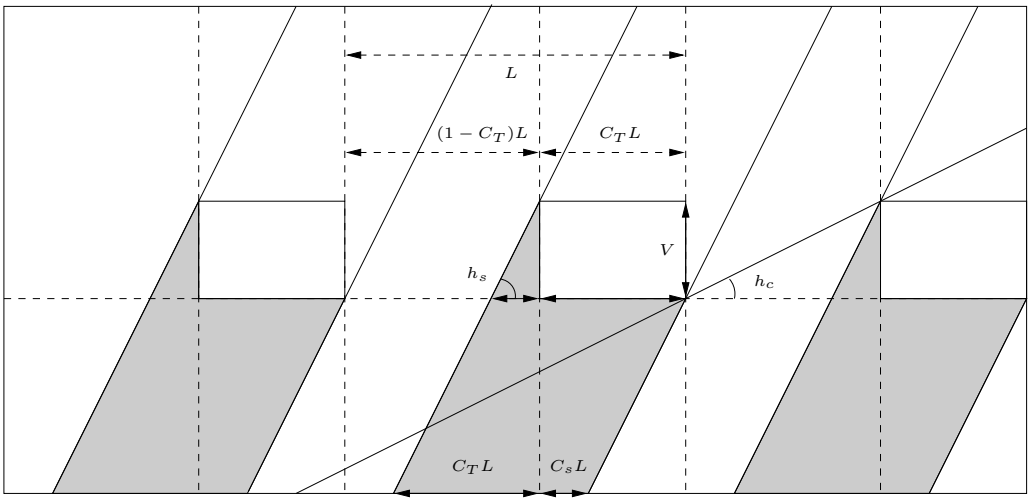

Figure 18: The screening effect of vertically extended clouds.

reaches a maximum for some intermediate cloud cover. Locally the effect can be considerable, e.g. close to a cloud having an extreme vertical extension. For example a cumulonimbus often have its base only a few hundred meters above ground but the top may penetrate the tropopause at 5,000–10,000 m. Close, but not below, such a cloud the coulisse effect may result in a considerable contribution to the cloud cover.

Let us illustrate the coulisse effect with a crude model in two dimensions, Figure 18. To get an estimate of the effect over a grid area, a uniform distribution of the clouds is assumed. All clouds are also restricted to one single layer with well defined base and top levels.

The side of each grid area is almost constant ($L \approx 22$ km) and the vertical cloud extension V can be estimated from the difference between the cloud top and base parameters.

If the solar elevation is below a critical value, the Sun does not shine directly on the ground. This value is given by

$$h_c = \arctan\left(\frac{V}{L(1 - C_T)}\right). \tag{26}$$

When the solar elevation is above h_c, a shadow is cast over parts of the clear area. Note that the rays from the Sun are parallel and that the height of the cloud base does not affect the result. The two shadows on the ground in the middle area correspond to a single shadow at the cloud base level. By putting the clouds on the ground we find the following simple formulation for the additional cloud amount C_s, due to the coulisse effect:

$$C_s = \frac{V}{L \tan(h_s)}. \tag{27}$$

Hence, given additional knowledge about the solar elevation it should be possible to model the effect of the vertical cloud extension and compile all cloud effects into one function t_b, in the same way as it was done for the global irradiance in section 4.2. The irradiance for the situation under consideration is then simply found by multiplying the clear sky irradiance value with the output from this function:

$$E_b = t_b(C_T, C_s, \rho_c, \rho_g, \rho_s)\, E_{b0} \tag{28}$$

Table 9: Estimates of the ratios between the cloud effect and the cloud transmittance for some typical cloud, ground (snow) and clear sky reflectances.

Spectral region	ρ_c	ρ_g (snow)	ρ_s	t_g/τ
Ultraviolet	0.60	0.050 (0.80)	0.35	1.3 (1.8)
Visible	0.60	0.10 (0.70)	0.20	1.2 (1.7)
Infrared	0.60	0.30 (0.30)	0.10	1.3 (1.3)

The sunshine duration is closely related to the direct solar irradiance since it is defined as the integrated time when the direct solar irradiance is larger than 120 W/m^2. Consequently, the sunshine duration (minutes / hour) should be possible to model using the same input parameters as was used for the direct component:

$$S_{dur} = 60 \cdot t_{dur}(C_T, C_s, \rho_c, \rho_g, \rho_s). \tag{29}$$

Note that the use of a separate cloud effect function, t_{dur}, for the sunshine duration allows us to calculate this quantity with a subhour resolution. This is not possible if the 120 W/m^2 threshold is applied directly to the hourly value of the direct irradiance.

4.4 Albedo and the cloud effect

It is important to note that the true cloud transmittance τ, defined as the ratio between the irradiance below and above the cloud, will generally differ from the cloud effect function t. For the direct irradiance we have for example included the coulisse effect in the cloud effect function and for the global irradiance the albedo of the sky, the ground and the clouds cause a difference. From equation (25) we have, for the overcast case:

$$\frac{t_g}{\tau} = \frac{1 - \rho_{s\lambda}\rho_{g\lambda}}{(1 - \rho_{s\lambda}\rho_{c\lambda})(1 - \rho_{c\lambda}\rho_{g\lambda})}. \tag{30}$$

The true cloud transmittance is probably almost independent of wavelength in the solar part of the spectrum, (Kylling et al., 1997). But, since the reflectance values are spectrally dependent the cloud effect will vary with wavelength. By inserting realistic values of the reflectances into equation (30) we get an idea of the ratio between the cloud effect and the cloud transmittance, Table 9.

The strongest influence appears in the visible and the UV range where the change in ground reflectance is large, when comparing bare ground to snow covered ground. In this case the increase in the cloud effect function amounts to about 40%. This illustrates that the surface reflectance is important and that it must be included in the cloud effect function.

The cloud reflectance is not described explicitly in the cloud effect model but some information connected to it should be available from the cloud top, cloud base and precipitation parameters. Considering the relatively large overall uncertainties connected to clouds the parameterisation will be simplified by the following assumptions. The effect of clouds is introduced spectrally only by the use of one cloud effect function for PAR and global radiation and another one for the UV region. Hence, the cloud effects are only applied to integrated irradiance values.

It is assumed that only the cloud effect functions for the direct component and the sunshine duration have a solar elevation dependence and that the dependencies from variations in the sky and in the ground reflectance are sufficiently small compared with other uncertainties. These effects are contained in the cloud effect as previously demonstrated.

4.5 Parameterisation of the cloud effect function

Traditional parameterisations are most often based on SYNOP information, using a few variables such as total cloud cover, cloud type and occurrence of precipitation. In our case we want to try and make use of the larger amount of information that is available from modern numerical weather prediction models and mesoscale analysis systems.

Since these systems produce lots of information that is not always compatible with SYNOP data it is necessary to come up with new parameterisations. In this situation neural networks are attractive since they provide us with a black box model alternative that can handle a large number of input parameters. Because of this we decided to model the cloud effect functions using feed forward neural networks. The reader is referred to (Haykin, 1999) for a thorough treatment of neural networks.

As noted in the previous section, the spectral dependence of the cloud effect is introduced by using one function for PAR and global irradiance, one for the UV irradiance and one for the direct radiation. For all but the direct component and the sunshine duration, the neural nets for the cloud effect t are parameterised as

$$E = t(C_T, C_L, P_b, H_b, H_t, p_{1h}) \cdot E_0 = t(w, x) \cdot E_0. \tag{31}$$

In the above equation w is the weight vector for the neural net. The components constituting the input vector x are given by the total- and low cloud cover (C_T and C_L), the cloud base probability (P_b), the cloud base and top (H_b and H_t) and the 1h precipitation (p_{1h}). The cloud effect for the direct component also includes the solar elevation which allows the network to model coulisse effect.

The neural nets all use 8 hidden units followed by a linear function which means that the function of the net is given by:

$$t(w, x) = w_1^T \, f(W_2 \, x + b_2) + \; b_1, \; f_i(x) = \frac{2}{1 + \exp(-2x)} - 1, \; i = 1, \ldots, 8 \tag{32}$$

where $t(w, x)$ is the output from the net, w_1 is an 8-dimensional vector of weights for the linear function, W_2 is a 8 $\times n$ matrix of weights for the hidden units (one row for each unit), x is the n-dimensional input vector and $f(\cdot)$ is a 8-dimensional vector valued function where each component $f_i(\cdot)$ corresponds to a sigmoidal hidden unit. The scalar b_1 and the 8-dimensional vector b_2 are so-called bias parameters that control the function behaviour when either x or f is zero.

The parameters in each net were estimated by minimisation of a quadratic measure $V(w)$ using the Levenberg-Marquardt method:

$$V(w) = \sum_i (E_i - t(w, x_i) \cdot E_{0i})^2. \tag{33}$$

The independent estimation and validation data sets for all but the UV cloud effect network are both made up of about 10,000 samples of hourly data from the year 1998 and

consist of measured irradiances E_i and input vectors x_i together with modelled clear sky irradiances E_{0i}.

In order to compare the measurements I_t, representing the irradiance integrated during the hour before t, with the instantaneous model output m_t at time t, the instantaneous value is approximated with a 3 point Gaussian mean value and the integrated value is approximated using the trapezoid method. This means that the instantaneous value at time t should be compared to the mean of the measurements valid for the hours before t and $t+1$:

$$m_t \approx \frac{m_{t-1}}{4} + \frac{m_t}{2} + \frac{m_{t+1}}{4} = \frac{1}{2}\left(\frac{m_{t-1}+m_t}{2} + \frac{m_t+m_{t+1}}{2}\right) \approx \frac{I_t + I_{t+1}}{2}. \qquad (34)$$

The global radiation data comes from all twelve stations in the SMHI radiation network while two stations, Karlstad and Kiruna, were excluded from the data set for direct irradiation and sunshine duration due malfunctioning suntrackers and pyrheliometers. Since information about the UV irradiance only was available from one station the estimation and validation datasets for the UV cloud effect function are smaller and consist of about 1,500 samples each.

The median value and the standard deviation of E/E_0 was calculated for 100 evenly spaced bins. Data points lying more than three standard deviations away from the median value were considered to be outliers. In order to force the cloud effect to 1 when the total cloud cover equals 0, the measurements E_i was set to the same value as the clear sky model E_{0i} whenever $C_T < 0.05$. The same procedure was applied to the direct radiation and the sunshine duration and in these cases also the overcast situation was modified by setting E_i to 0 whenever $C_T > 0.99$. The reason for doing this is the scale difference problem. Measurements are point values while the model is supposed to make statements on the mesoscale. The model need to be consistent on the right scale and here this means being consistent with the information about the total cloud amount. This problem is discussed in more detail in section 6.

In the following sections the resulting black box parameterisation of the cloud effect is compared to traditional ones and interpreted in terms of total cloud amount and cloud type.

4.6 Comparison with SYNOP cloud relations

The total amount of clouds is the most important variable in the cloud effect function. It is worth noting that the traditional SYNOP cloud amounts based on manual observations under certain conditions systematically differ from the amounts as observed from satellite based platforms or obtained by ceilometers (laser). For example, in case of a broken cloud cover with vertically extended cumulus clouds, the manual observer viewing the sky dome will also partly include the sides of the clouds in the cloud amount. The other two methods, on the other hand, mostly see the tops or the bases as projected on a horizontal plane.

There are also other inconsistencies between the various methods to observe the cloud cover. The laser instruments in the present observation network cannot see high clouds. They may be too high and out of range or obscured by lower cloud layers. The satellite based instruments only observe the cloud tops and the interpretation of the observed radiances may sometimes be erroneous. The MESAN algorithms try to combine a number of sources to benefit from the best available information. Examples of frequency distributions for the total cloud amount as given by MESAN are presented in Figure 19. Here,

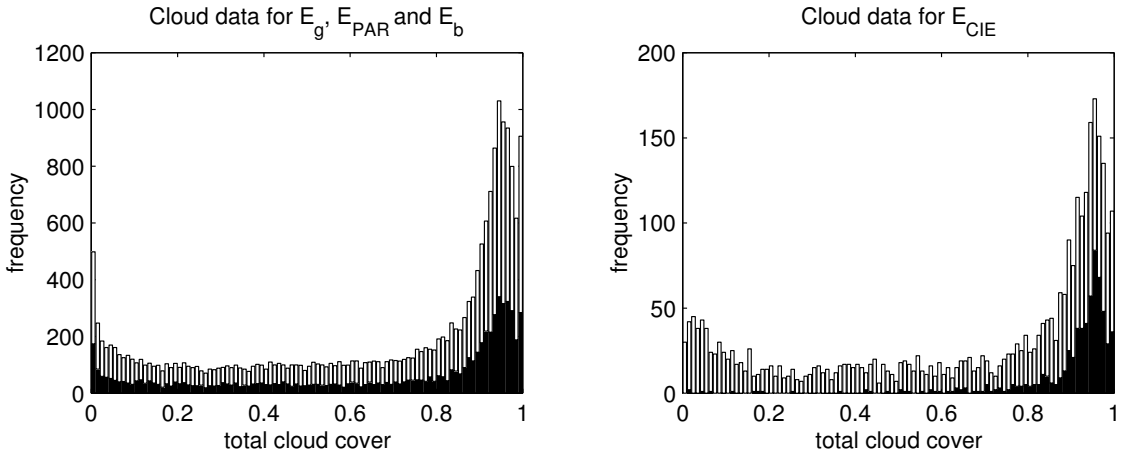

Figure 19: Left: Histogram for the total cloud amount in the estimation and validation data set of the cloud effect function for global radiation, PAR and direct radiation. The black part of the histogram refer to precipitating clouds and the white part to non-precipitating clouds. Right: The same for the dataset regarding the cloud effect function for UV radiation.

100 categories or bins, representing evenly spaced amounts of cloud cover, were used for the accumulation of the frequencies. Note that the u-shape of the histogram which is well known from SYNOP clouds is also a feature for the MESAN clouds. There is a bias towards the overcast end of the histogram where there is also a peculiar and sudden drop in the frequencies.

As a user one should remember that the data consistency and quality varies. Direct inter-comparisons with the traditional cloud parameters could be done noting the inconsistency and limitations. An example of existing inconsistency in the MESAN is that the total cloud amount may sometimes be less than the amount of low clouds. The reason for this can be explained as the low cloud amount is mainly based on information retrieved from surface based observations while the total cloud amount often is based on satellite information. Surface observations are made at specific points and the data have to be interpolated to a grid. Satellite data have a good spatial coverage and information about areas between the surface sites is usually available. Within the MESAN project it has not been decided which one should be regarded as the best estimate in case of an inconsistency. In this application we have decided to give higher priority to the total cloud amount and truncate the amount of low clouds when necessary.

4.6.1 Cloud effect as a function of total cloud amount

When the simple physical model for the irradiance under a broken cloud cover was presented in section 4.2.3, it was assumed that the irradiance in this case could be obtained as a linear combination of the irradiance in clear and overcast cases using the total cloud cover as the weight.

It is well known that a linear relation such as the one in equation (25) does not fit available measurements. However, the way global radiation depends on the total amount of SYNOP clouds has been shown to be accurately described by other simple functions, (Kasten and Czeplak, 1980). One example of such a cloud effect function is given by

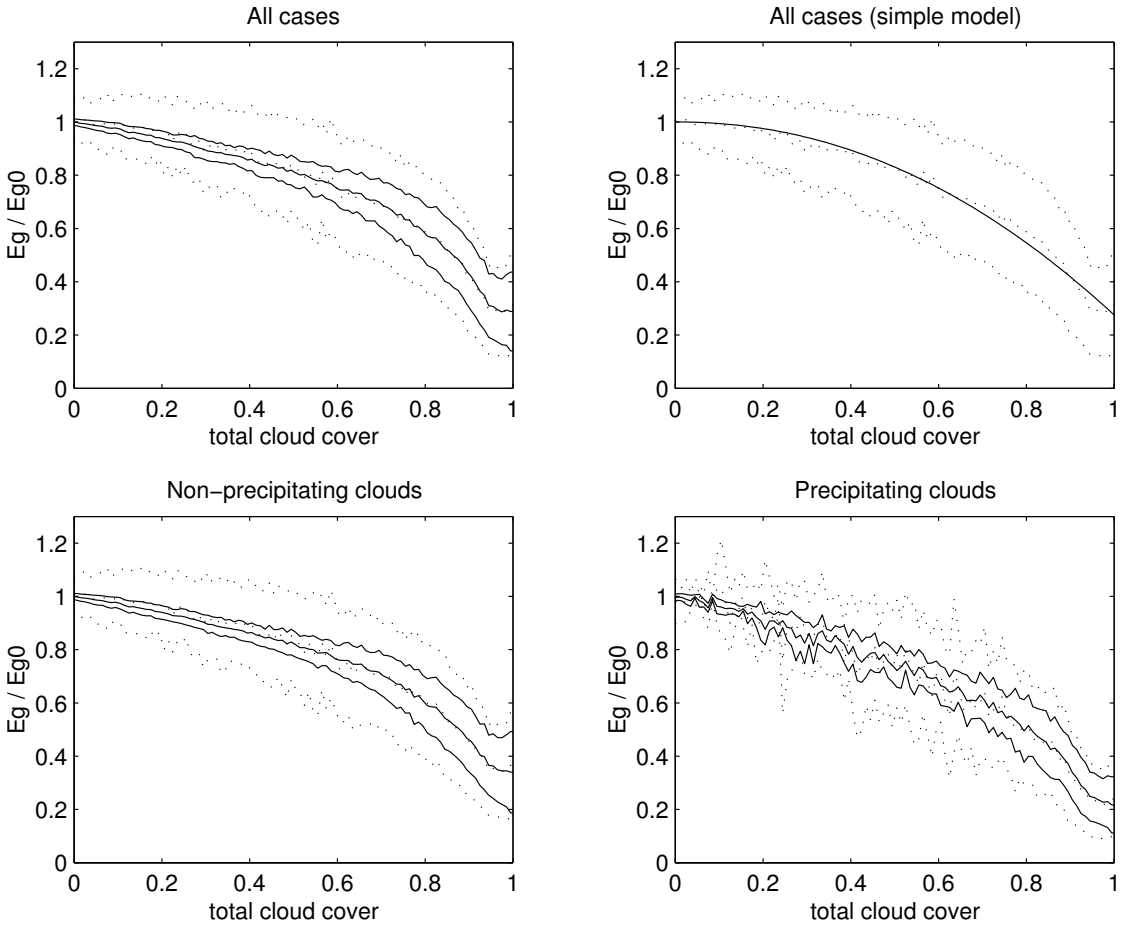

Figure 20: Cloud effect for the global radiation and PAR plotted against total cloud amount. Solid lines represents modelled mean values along with the one σ deviations. Dotted lines indicate measured values. Top left: the relation for all clouds. Top right: using the simple model described by equation 35. Bottom left and right: the same as in the top left panel but separated into non-precipitating and precipitating cases.

$$t(C_T) = 1 - (1 - t(1))\, C_T^{\alpha} \tag{35}$$

where C_T is the total cloud amount, $t(1)$ is the estimated cloud effect for overcast skies and the exponent α is a constant that also needs to be estimated from data.

Global radiation and PAR A comparison between the output from a cloud effect function on the form of equation (35) and our neural network for global and PAR radiation is shown in Figure 20. The top left panel illustrates the mean cloud effect and its standard deviation for the neural net (solid lines) and for the measurements (dotted lines). Mean and standard deviation values are calculated for the same 100 bins that were used for the accumulation of the histogram presented in Figure 19. It is evident that the model can explain some extra variance with the aid of input variables other than just the total cloud amount. Note that the cloud effect saturates for high cloud amounts and that this is captured by the model.

The simple model has total cloud amount as its only variable and therefore there is no variance with respect to other information as can be seen in the upper right panel. It is also unable to mimic the saturation at high values in the total cloud cover.

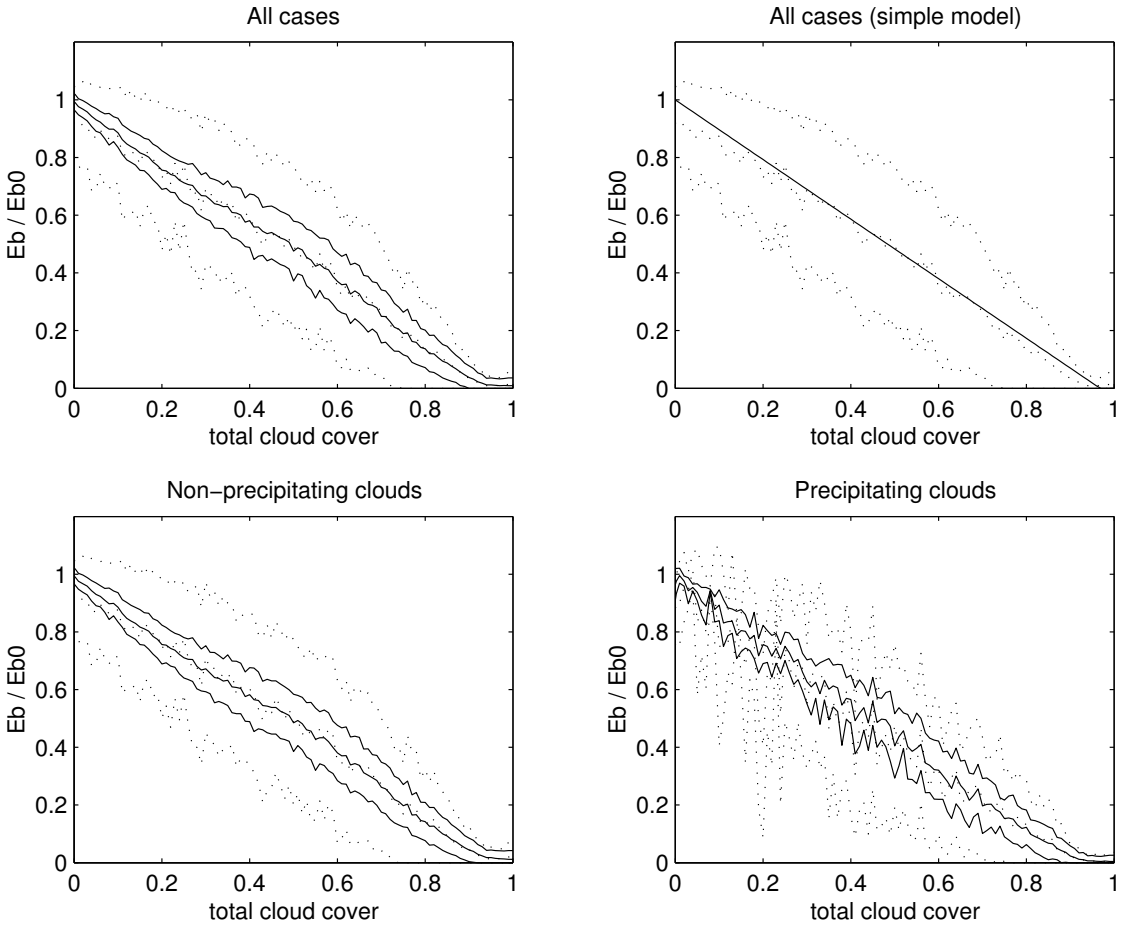

Figure 21: Cloud effect for the direct radiation plotted against total cloud amount. Solid lines represents modelled mean values along with the one σ deviations. Dotted lines indicate measured values. Top left: the relation for all clouds. Top right: using the model given by equation 35. Bottom left and right: the same as in the top left panel but separated into non-precipitating and precipitating clouds.

In the two lower panels the cloud effect is illustrated for non-precipitating (left) and precipitating (right) clouds. For precipitating clouds the cloud effect respond more rapidly to the total cloud cover and reaches a lower value for overcast situations as compared to the non-precipitating case. This effect is successfully reproduced by the model. In overcast situations the modelled mean value of the cloud effect is 0.29 (0.31), 0.34 (0.37) and 0.22 (0.24) for all cases, non-precipitating ones and precipitating ones respectively (measured values in parenthesis). As one would expect, precipitating clouds attenuate radiation more than non-precipitating ones do.

Direct radiation Figure 21 shows the the output from the cloud effect functions for the direct component. Again the top left panel illustrates the mean cloud effect and its standard deviation for the neural net (solid lines) and for the measurements (dotted lines). Also in this case the model succeeds to explain some extra variance with the aid of other input variables than the total cloud amount. Here the saturation of the cloud effect is more pronounced than for the global radiation and it is reproduced well by the model.

Even though the simple model structure based on equation (35) is able to capture the mean behavior and even the saturation (because it is truncated to zero) it suffers from not

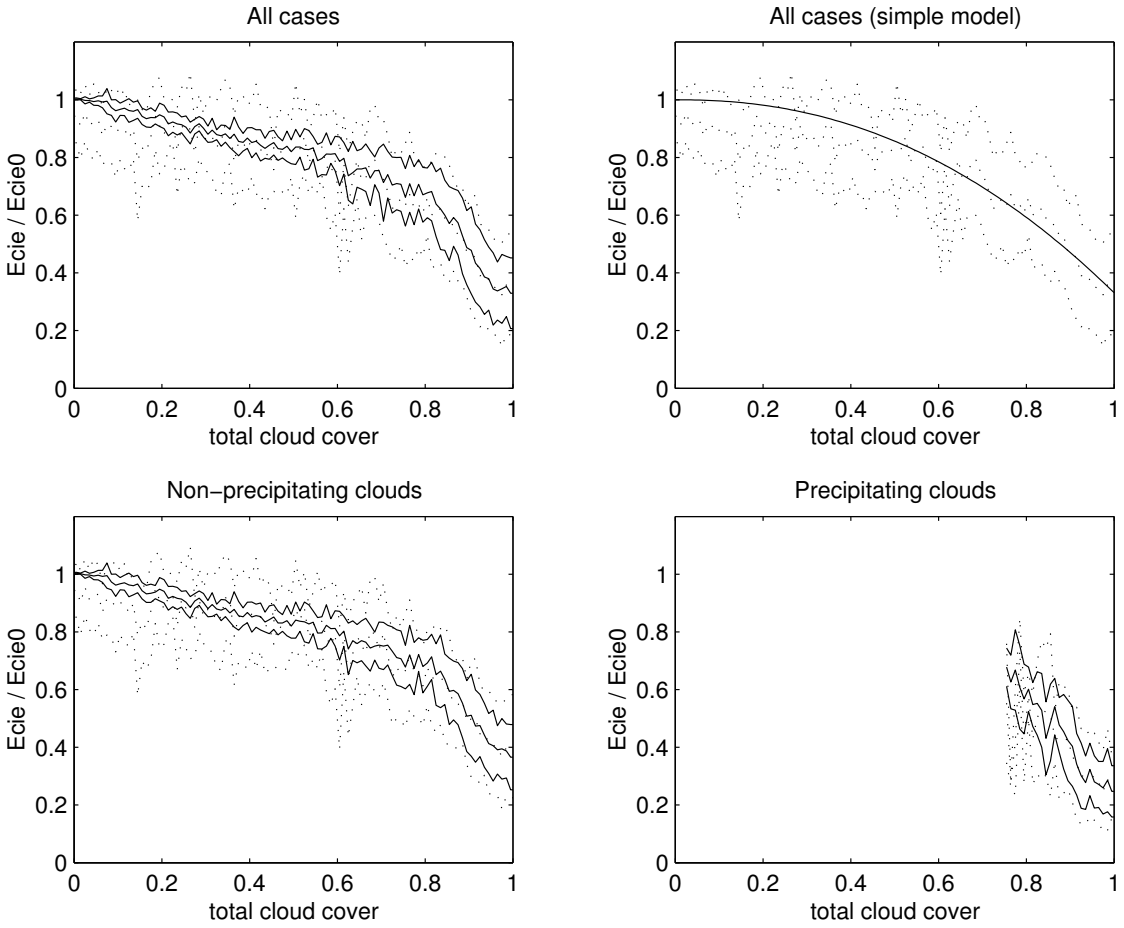

Figure 22: Cloud effect for the UV radiation plotted against total cloud amount. Solid lines represents modelled mean values along with the one σ deviations. Dotted lines indicate measured values. Top left: the relation for all clouds. Top right: using the model in equation 35. Bottom left and right: the same as in the top left panel but separated into non-precipitating and precipitating clouds. Note that only cases where $C_T > 0.75$ are shown in the right panel.

being able to explain any variance with respect to changes in other variables than the total cloud amount.

The distinction between precipitating and non-precipitating situations is not as distinctive here as in the case of global radiation. For the direct radiation most clouds acts more or less like an on-off switch.

UV radiation Finally the output from two cloud effect function for the UV radiation are studied. One is based on equation (35) and the other is produced by our neural network. The results are presented in Figure 22. In the top left panel where the mean cloud effect and its standard deviation for the neural net (solid lines) and for the measurements (dotted lines) are shown it can be noted that the saturation for high cloud amounts is less pronounced compared to the global radiation case.

Also in this case the simple model is given by equation 35. This means that it only depends on the total cloud amount and it is hence unable to capture any variance with respect to other information, Figure 22 top right.

Like in the previous cases the two lower panels display the cloud effect for non-

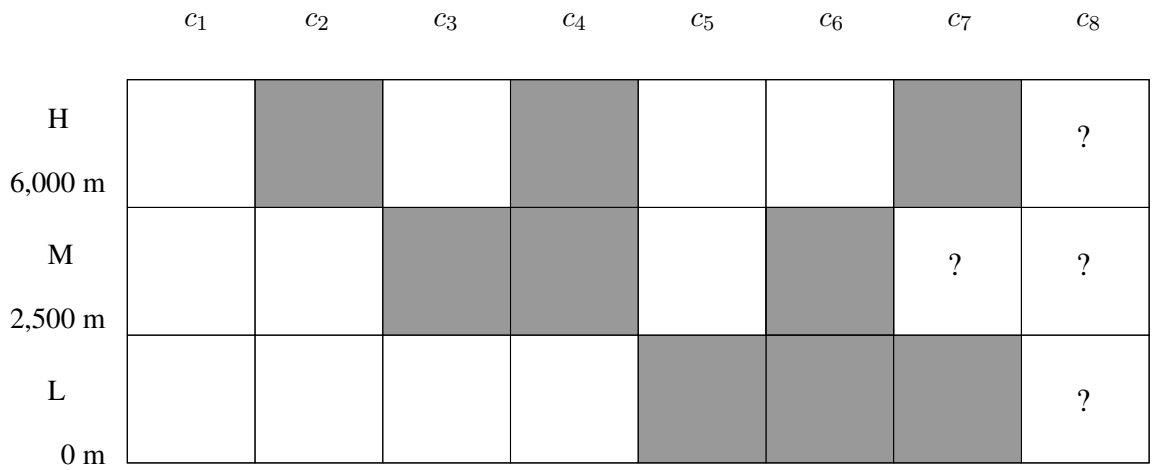

Figure 23: Classification of MESAN clouds into eight categories c_i based on cloud base and cloud top. Gray boxes indicate clouds while question marks denote uncertain regions.

precipitating (left) and precipitating (right) clouds. Since the number of samples in the UV data set is limited, only cases with precipitation in conjunction with a cloud cover above 0.75 are considered in the statistics. Note that precipitation tends to amplify the cloud effect and that the model is able to reproduce this behaviour. For overcast situations the modelled mean value (measured values in parenthesis) of the UV cloud effect is 0.33 (0.36), 0.37 (0.40) and 0.25 (0.26) for all cases, non-precipitating ones and precipitating ones respectively.

As noted previously it is not the cloud transmittance which is modelled since other effects such as the multiple reflection between the sky, the clouds and the ground are also included. Because of the varying effective reflectance in different spectral regions this factor will differ when comparing the effect for the total spectrum to that in the UV region. If we look at the cloud effect in overcast situations it turns out that clouds tend to decrease UV radiation less (1.0-0.36=64%) than global radiation (1.0-0.31=69%). This is in accordance with the findings reported in (Josefsson and Landelius, 2000).

4.6.2 Cloud effect as a function of cloud type

In the previous section the cloud effect was investigated with respect to total cloud amount and the occurrence of precipitation. In classical meteorological observation terminology clouds are classified in three layers and in a number of cloud types. There are a number of studies on global radiation where the cloud effect has been retrieved for these cloud types as well as for various amounts, (Haurwitz, 1948; Kasten and Czeplak, 1980; Davies et al., 1985).

Using MESAN it is not possible to exactly follow the classical scheme. However, in MESAN there are some remnants from the division into three cloud level categories. The amount of low clouds is defined for cloud bases below 2,500 m, which is about the classical limit for the class of low clouds. Using the information in the top and base parameters it should be possible to approximately follow the old classification. One advantage of doing this will be the possibility for comparing with the available studies. When the total amount of clouds is less than $3/8$ there is no cloud top or cloud base defined in MESAN. This condition defines the cloud free class which will thus often be contaminated by clouds.

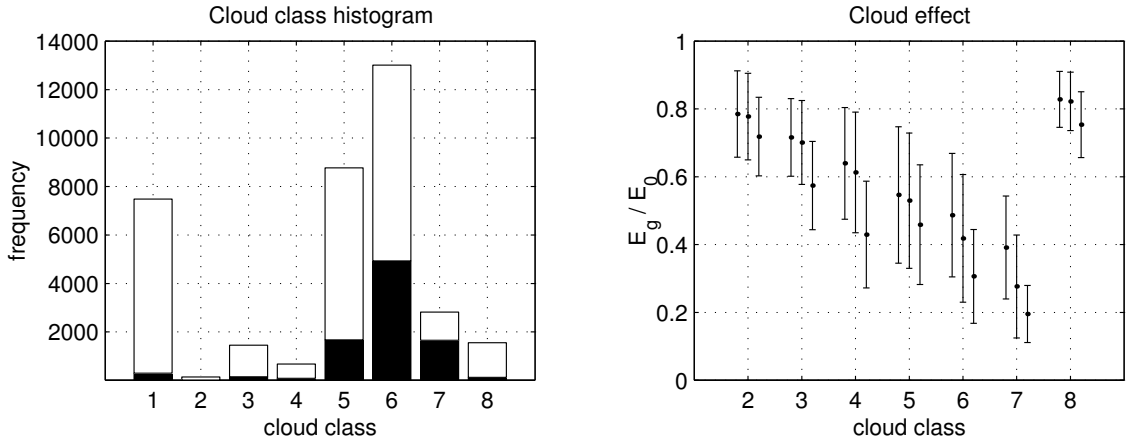

Figure 24: Left: Histogram for the eight cloud classes. Black bars relate to precipitating clouds and white ones to non-precipitating clouds. Right: Cloud effects for each class (mean and standard deviations) divided into non-precipitating (left bar), all (middle bar) and precipitating clouds (right bar).

Following this approach we end up with eight classes where the last one is used for outliers. The classes and their corresponding cloud types are illustrated in Figure 23 and a short explanation of each class is given below. A histogram with information about the class frequencies for precipitating and non-precipitating cases is shown in Figure 24.

Class 1 is the clear or almost cloud free class. It is defined by the condition $C_T < 3/8$, corresponding to less than 3 oktas (eights), which for the classical synoptic meteorological observations was the level when cloud amounts became significant. In this case the top and base are undefined.

Class 2 is dominated by high level clouds, i.e. both the cloud top and base are above 6,000 m. There might exist some lower clouds of insignificant amount, i.e. $C_L < 3/8$.

Class 3 is characterised by middle level clouds. In this case the cloud top has to be lower than 6,000 m and the base has to be heigher than 2,500 m, which fits the traditional definition of middle level clouds. Again, there might exist small amounts of low level clouds.

Class 4 mainly contains middle and high level clouds. Here the top is above 6,000 m and the base must be above 2,500 m but below 6,000 m. Small amounts of low clouds are neglected. It is not possible to differentiate between one extended layer and two or more cloud layers. If more than one layer exists, it will not only be the number of layers that are unknown. Also the amount within each layer will be out of reach.

Class 5 is dominated by low level clouds. In this case the top is below 2,500 m, which defines the limit for middle level clouds. There might exist some high and middle level clouds of insignificant amount $C < 3/8$ which are ignored.

Class 6 mostly contains low and middle level clouds. In this case the top is higher than 2,500 m but lower than 6,000 m. The base has to be below 2,500 m. High level clouds of small amounts are assumed to be neglectable.

Table 10: Climatological values for the cloud effect on global irradiance for different cloud types as reported by Kasten & Czeplak for Hamburg and by Davies et al. for Canada. The range for the data from Davies et al. and our model corresponds to the one sigma interval. Only cases where $C_T > 0.975$ are considered from our model.

Cloud type	K & C	Davies et al.	Our model	Class
Ci, Cs, Cc	0.61	0.80 ± 0.05	0.54 ± 0.04	c_2
Ac, As	0.27	0.39 ± 0.06	0.49 ± 0.09	$c_3 - c_4$
Ns	0.16		0.22 ± 0.10	$c_3(p) - c_7(p)$
Sc, Cu	0.25	0.29 ± 0.01	0.29 ± 0.12	c_5
St	0.18			
All	0.25		0.29 ± 0.14	$c_2 - c_8$

Class 7 probably contains clouds at all levels. In this case the top is above 6,000 m and the base is below 2,500 m. This tells us that there are clouds from the bottom to the top of the atmosphere. It is, however, impossible to say whether we are dealing with extremely extended low level clouds or several cloud layers.

Class 8 is a class containing what is not in the other classes. It is used for erroneous cases when there is no signigicant cloud base even though $C_T > 3/8$ or when the cloud base is said to be higher than the cloud top.

Some of these cloud classes, defined using MESAN information, are similar to those in classical meteorology and the cloud effect our model predict for these classes can thus be compared to values found in literature, e.g. (Kasten and Czeplak, 1980) for Hamburg and by (Davies et al., 1985) for Canadian stations using the method of Kasten and Czeplak. Note that the cloud type in these two studies is determined from ground based observations which makes it hard to differ between cloud classes with the same cloud base. This is the reason why we use combined classes in the comparison. Both the values from the study of (Davies et al., 1985) and our model are given together with the standard deviations in Table 10. The variation within each class indicates that one could expect rather large uncertainties in individual model values if climatological values are used to calculate the cloud effect based on these cloud classes.

The relativily large discrepancies for clouds belonging to class c_2 could partly be explained by the small number of data making up this classes, see the right panel in Figure 24. Mean and standard deviations for the cloud effects of each class is given in the right panel of the same figure. The three bars denote, from left to right, non-precipitating, all clouds and precipitating clouds. Note that the cloud effect is rather high for the outliers constituing class c_8. This seems reasonable since this class contains cases with insignificant or high cloud bases.

The study of Davies et al. also suggests that the seasonal and regional variations within Canada are small and can be neglected. However, it cannot be excluded that climatological differences may exist between Europe and Canada. Looking at the Hamburg data in Table 10 it seems as if the clouds in Europe are optically denser. This could perhaps also be explanined by differences in the way the cloudiness was observed.

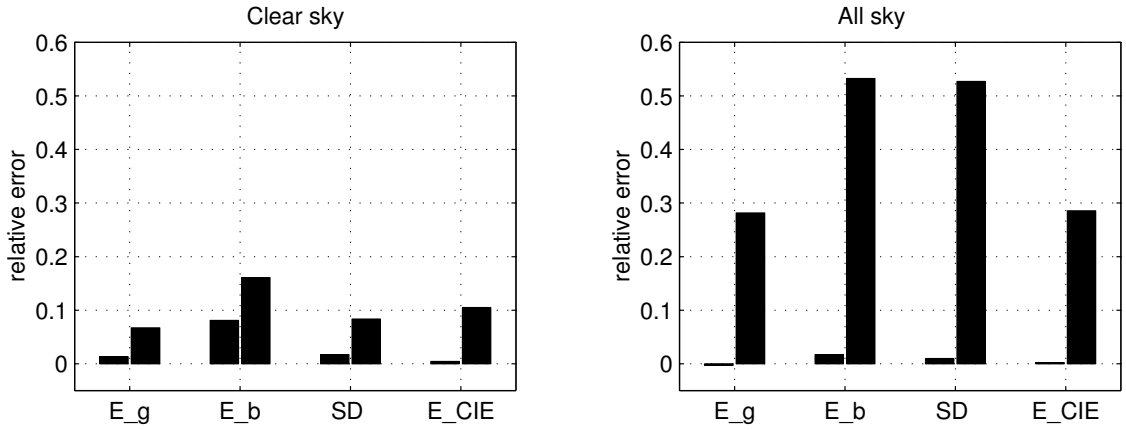

Figure 25: MBE and RMSE under clear (left) and all (right) sky conditions for global- (E_g) and direct radiation (E_b) together with sunshine duration (SD) and UV radiation (E_{CIE}).

5 Model validation

In the previous section cloud effect models for different kinds of radiation were produced and their parameters estimated. However, the main purpose of this model system is to model the radiation quantities themselves and in this section the model system is validated from that perspective. The same independent validation sets that were used in the parameter estimation procedure for the cloud effect models are reused here. The MBE is calculated as the mean difference between modelled and measured values so a negative MBE means that the model underestimates the given quantity.

The model output is validated on different time scales and with respect to the geographic locations in the SMHI radiation network. Also the difference in model performance between clear and cloudy situations is investigated. Finally frequency distributions and output field examples are given for each of the modelled radiation quantities.

5.1 Global radiation

The MBE and RMSE in the modelled hourly global irradiance for clear and all skies are shown in Figure 25. For the clear sky case the MBE is 1.3% (3.4 W/m^2) and the RMSE is 6.7% (18 W/m^2) which are similar but smaller values than those presented for the clear sky model in section 3.2. Here, however, the cloud effect function has been allowed to affect the output from the clear sky model. For the general case the MBE decreases to -0.28% (-0.62 W/m^2) and the RMSE increases to 28% (63 W/m^2). Note that the validation period used here (February–December 1998, 10,697 samples) is different from the one used for the clear sky model (April–September 1998) which results in the errors being related to a lower mean value.

These figures can be compared to the results from a much simpler model. Consider using only the total cloudiness and a cloud effect model according to Kasten's function in equation (35). Such a procedure increases the RMSE from 28% to 35% for hourly values of global radiation.

A geographical view of the errors is given in Figure 26 where the MBE and RMSE for the modelled global irradiance is shown for the twelve stations in the SMHI radiation network. The stations are given in decreasing latitude order, from left to right beginning

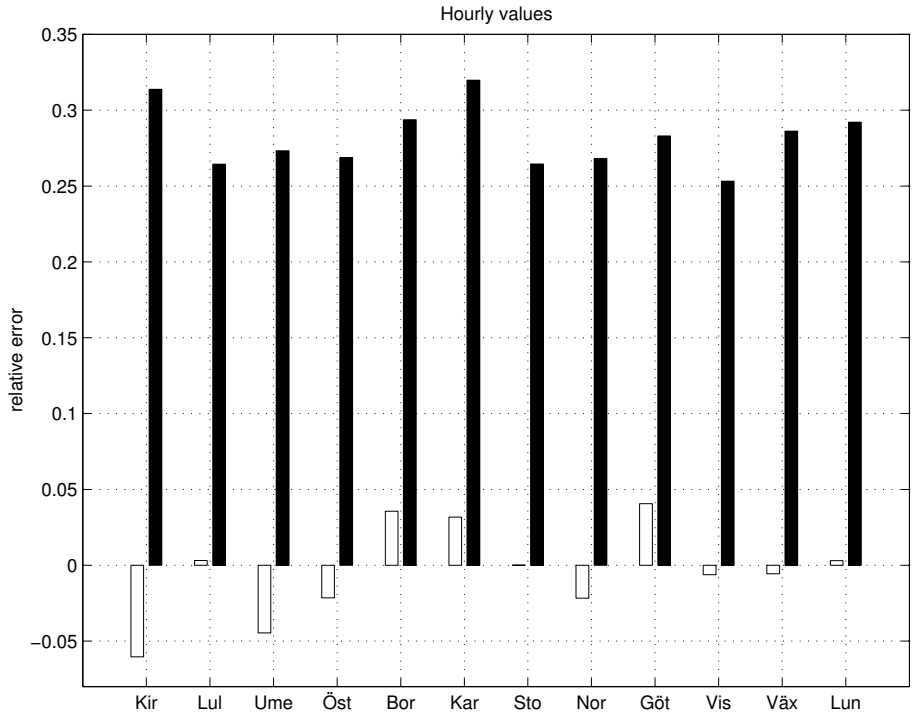

Figure 26: Geographical error (white bars for the MBE and black ones for the RMSE) distribution of the modelled global irradiance at the SMHI radiation network stations from Kiruna in the north (left) to Lund in the south (right).

with Kiruna, 67.83° N and ending with Lund, 55.72° N. The relatively large MBE in Kiruna can only to a small extent (about 1%) be explained by the presence of snow and the fact that a constant albedo of 0.2 was used in the model simulations. The minimal and maximal RMSE values are 25% (Visby) and 32% (Kiruna) respectively. A reasonable explanation for this difference may be attributed to the variation in cloud cover. During the validation period the mean total cloud cover was 78% in Kiruna but only 63% in Visby.

An illustration of the frequency distributions for the modelled (black thin bars) and measured (white bars) global irradiances are given at the bottom left of Figure 27. The general agreement between the two distributions is good and the only difference is that the lowest values come out a bit too high in the model.

Modelled and measuerd hourly global irradiance values (validation data) are plotted against each other in a scatterogram at the bottom left of Figure 28. The correlation between the two sets is 0.94.

To give an impression of the impact of the cloud effect function an example of the model output field is given in Figure 29. In order to facilitate a comparison with the clear sky example from Figure 13 the same date and scales are used in both cases.

Estimates of the MBE and RMSE for daily and monthly values of global radiation are presented in Figure 30. In this case the daily MBE and RMSE are -0.15% and 16% while the monthly MBE and RMSE are -0.15% and 5.7%.

An illustration of the evolution of modelled daily global irradiance estimates is given at the top left in Figure 31. The example is taken from the station in Norrköping during February–December 1998. In this case the model was applied to all samples in order to produce a continuous curve. Note, however, that there is a wide gap in the data aorund June when the model data collection system was down.

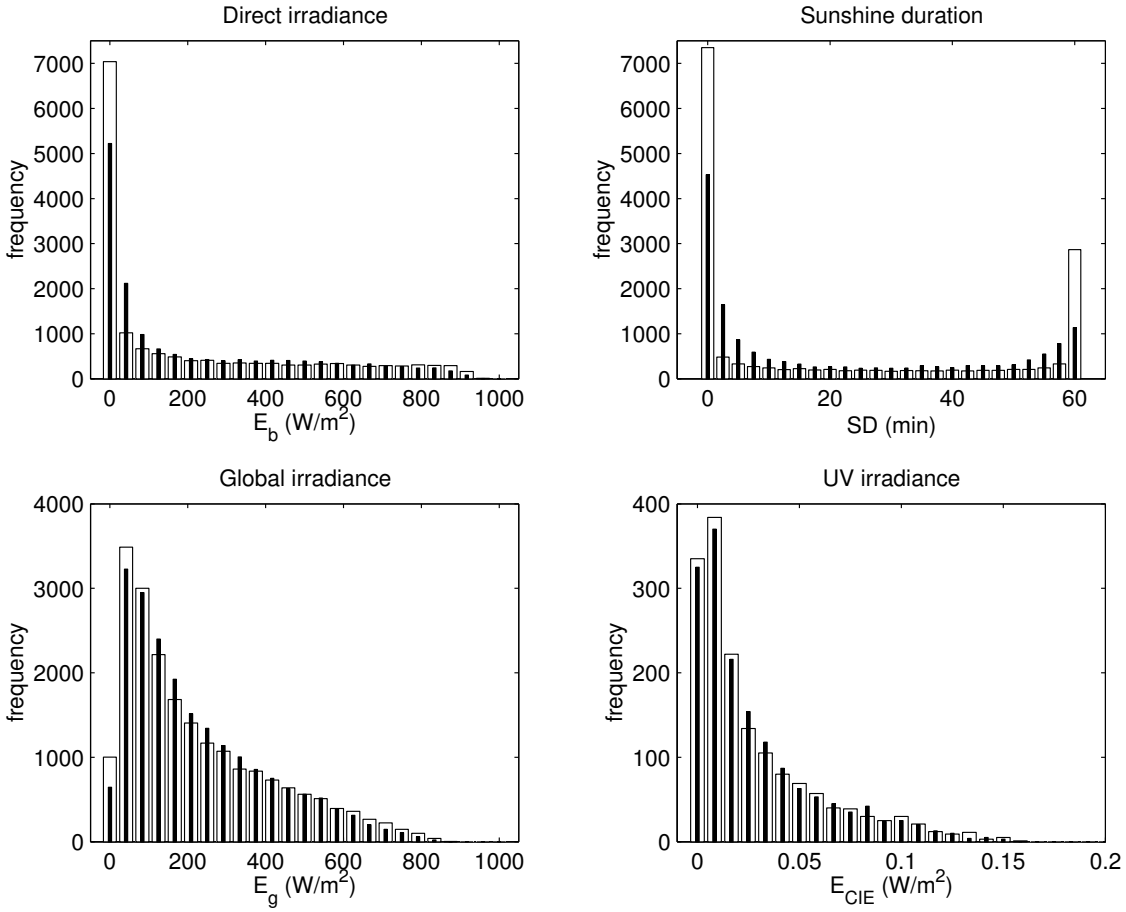

Figure 27: Histograms for hourly values of some modelled (black thin bars) and measured (white bars) radiation quantities. Top left: direct irradiance. Top right: sunshine duration. Bottom left: global irradiance. Bottom right: CIE UV.

5.2 Direct radiation

The direct radiation under a cloudy sky is hard to model for the same reasons as mentioned in connection with the parameterisation of the cloud effect. Compared to the global radation, the RMSE for the modelled direct irradiance under cloudy conditions is about twice as high. The validation results for clear and cloudy cases are presented in Figure 25. In case of a clear sky case the MBE is 8.1% (56 W/m^2) and the RMSE is 16% (110 W/m^2) which are about half the values presented for the clear sky model in section 3.2. However, there is a difference in that the cloud effect function has been applied to the output from the clear sky model. For the general case the MBE decreases to 1.7% (3.7 W/m^2) and the RMSE increases to 53% (still 110 W/m^2). Note that the validation period here is February–December 1998 which results in the errors being related to a lower mean value.

These results can again be compared to the error obtained if a cloud effect model based on equation (35) would be employed. In that case the RMSE for the hourly direct irradiance increases from 53% to 59%.

The frequency distributions for the modelled (black thin bars) and measured (white bars) direct irradiances are illustrated at the top left of Figure 27. As for the global radiation, the overall correspondence between the distributions for the modelled and the measured irradiances is good. The only difference seem to be that really low values are overestimated by the model.

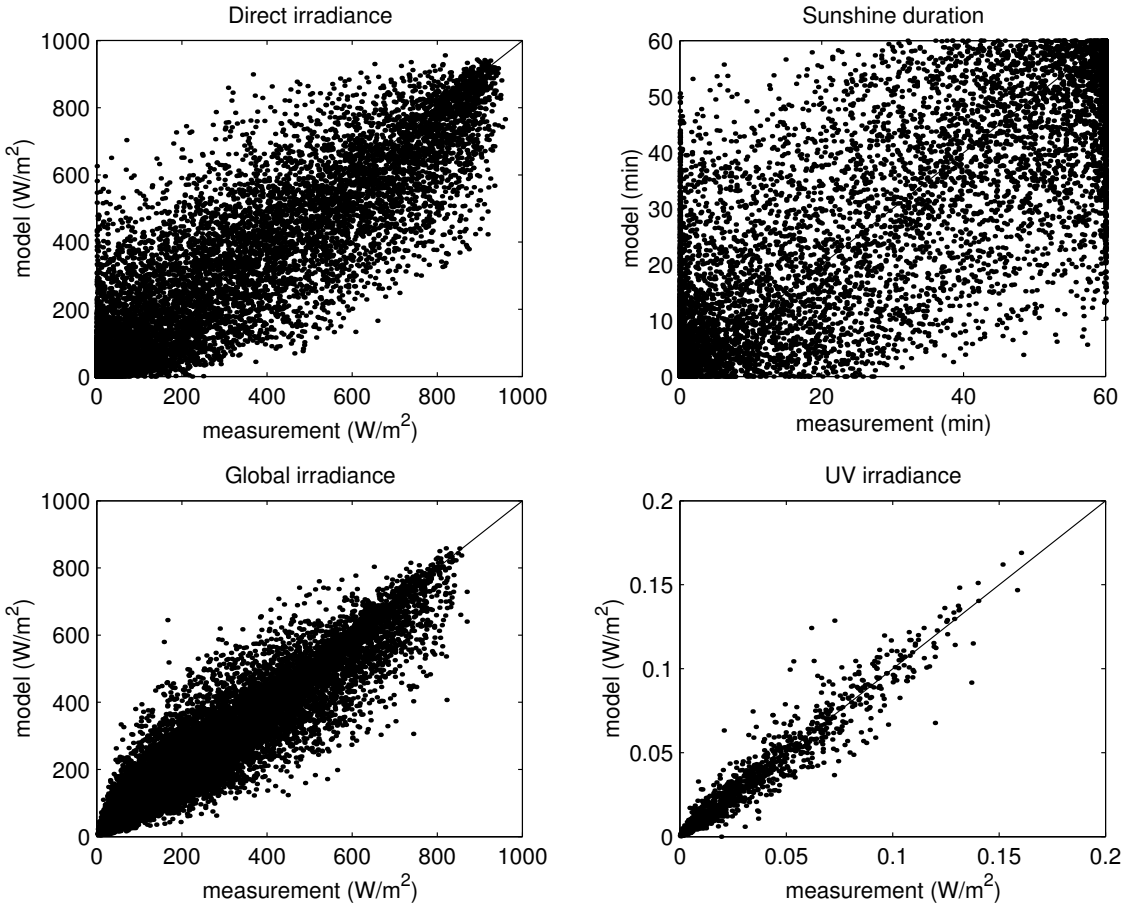

Figure 28: Scatterplots for hourly values of the direct irradiance (top left), sunshine duration (top right), global irradiance (bottom left) and the UV irradiance (bottom right).

The correlation between modelled and measuerd hourly direct irradiance values (validation data) amounts to 0.91. A scatterogram showing the the two sets plotted against each other is given at the top left of Figure 28.

The impact of the cloud effect function on the direct irradiance is examplified by the model output field in Figure 29. In order to make a comparison with the clear sky example from Figure 13 easier, the same date and scales are used in both cases.

A time series with modelled daily direct irradiance values at Norrköping, during February–December 1998, is presented at the top right of Figure 31. Here the model was applied to all samples in order to produce a continuous curve. Despite this there is a wide gap in the data around June when the model data collection system was down.

Validation results in terms of MBE and RMSE for daily and monthly values of direct radiation are presented in Figure 30. The daily MBE and RMSE are 2.1% and 31% while the monthly MBE and RMSE are 2.1% and 11%.

5.3 Sunshine duration

The sunshine duration is closely related to the direct irradiance and the validation results for these two quantities are indeed similar. There is, however, a difference between the two in case of a clear sky, as illustrated in Figure 25. The lower errors for the sunshine duration may be explained by the fact that sunshine duration is a coarser measure than the direct irradiance since it is defined as the number of minutes per hour when the direct

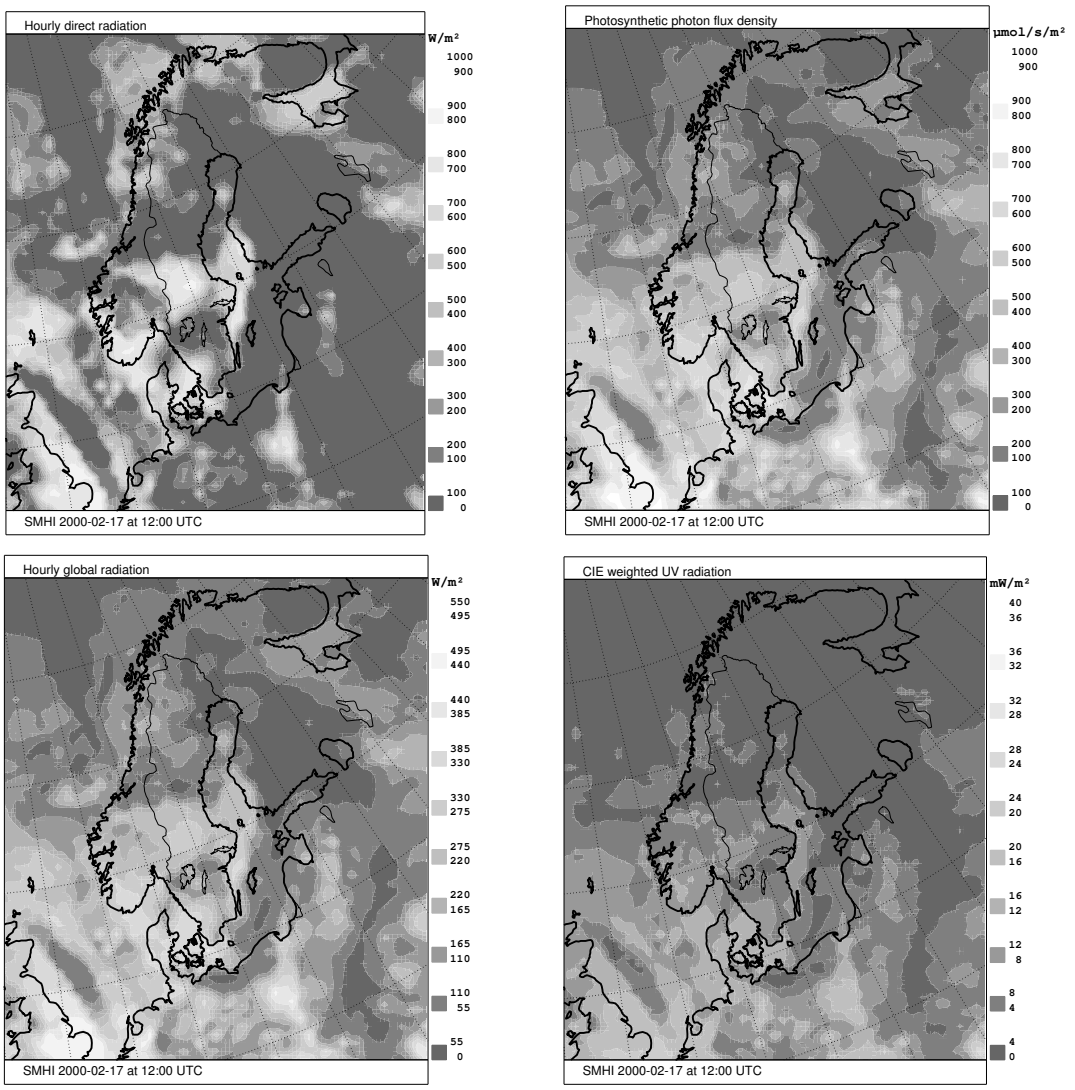

Figure 29: Hourly model fields of global radiation (top left), PAR (top right), direct radiation (bottom left) and CIE UV (bottom right). All fields refer to the date February 17, 2000 at 12:00 UTC.

irradiance exceeds 120 W/m^2. For the clear sky case the MBE is 1.7% (1.0 min) and the RMSE is 8.3% (4.9 min). In the general case the MBE decreases to 0.98% (0.20 min) and the RMSE increases to 53% (11 min). Please note that the mean value changes between clear and cloudy situations.

Let us consider using only information about the total cloudiness and model the cloud effect for the sunshine duration according to equation (35). This would lead to an increase in the RMSE from 53% to 58% for the hourly values.

A histogram for the hourly sunshine duration estimates is given at the top right of Figure 27 where modelled and measured values are represented with black and white bars repspectively. The U-shaped frequency distribution is similar to the one obtained for the total cloud cover in Figure 19. A difference between the distributions for the modelled and the measured quantities is that the histogram for the modelled values is smoother.

The two peaks at zero and sixty minutes are also seen clearly in the scatterplot of the two sets at the top right of Figure 28. The correlation between modelled and measuerd

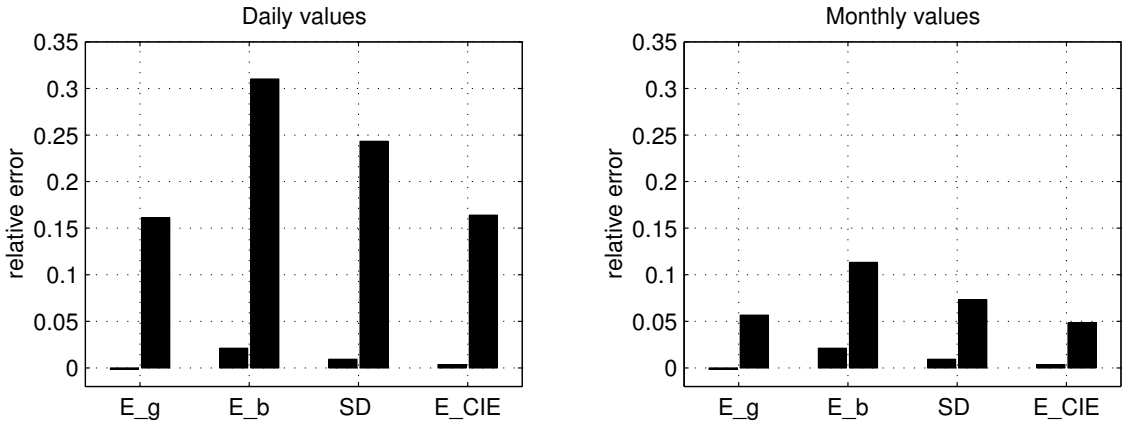

Figure 30: Daily (left) and monthly (right) MBE and RMSE for global- (E_g) and direct radiation (E_b) together with sunshine duration (SD) and UV radiation (E_{CIE}).

sunshine duration values (validation data) amounts to 0.90.

An example with modelled daily sunshine duration estimates is given at the bottom left in Figure 31. The data comes from the station in Norrköping during February–December 1998. In order to produce a continuous curve the model was applied both to estimation and validation data. The wide gap around June was due to problems with the model data collection system.

Figure 30 presents the validation results in terms of MBE and RMSE for daily and monthly values of sunhine duration. The daily MBE and RMSE are 0.92% and 24% while the monthly MBE and RMSE are 0.92% and 7.3% respectively.

5.4 UV radiation

The validation data set for the CIE UV is smaller than for the other radiation quantities since measurements are confined to the station in Norrköping.

The MBE and RMSE in the modelled hourly UV irradiance for clear and all skies are shown at the bottom right in Figure 25. For the clear sky case the MBE is 0.45% (0.21 mW/m^2) and the RMSE is 10% (5.0 mW/m^2) but the statistical significance can be questioned since the number of clear sky cases only amounts to 47 samples. For the general case the number of samples is 1,616 and here the MBE decreases to 0.21% (0.058 mW/m^2) and the RMSE becomes 29% (7.9 mW/m^2). In this case the statistics are more reliable and the errors are comparable to those obtained for the global radiation. For the CIE UV switching to a simpler model, based only on the total cloudiness, causes the RMSE to increase from 29% to 36% for the hourly values.

The agreement between the frequency distributions for the modelled (black thin bars) and measured (white bars) hourly UV irradiances is good, as can be seen at the bottom right in Figure 27.

Modelled and measuerd hourly UV irradiance values (validation data) are plotted against each other in a scatterogram at the bottom right of Figure 28. The correlation between the two sets is 0.97.

To illustrate the effect of the cloud effect function and to give an example of what the model output look like, an output field is given in Figure 29. In order to facilitate a comparison with the clear sky example from Figure 13 the same date and scales are used in both cases.

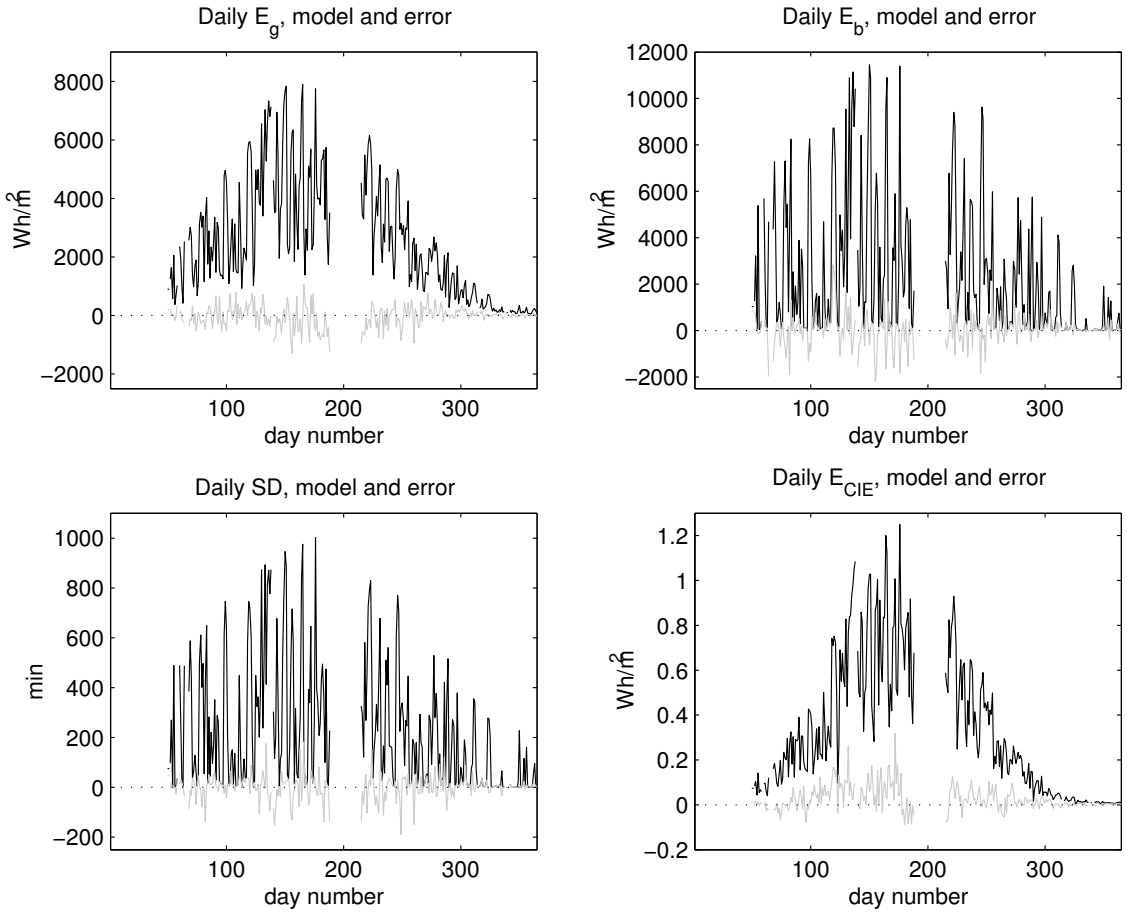

Figure 31: Examples of modelled daily radiation quantities (black) at Norrköping together with error estimates (gray). Top left: global irradiance. Top right: direct irradiance. Bottom left: sunshine duration. Bottom right: CIE UV.

A time series with daily UV irradiance estimates is given at the bottom right in Figure 31. The example is taken from the station in Norrköping during February–December 1998. In this case the model was applied to all samples in order to produce a continuous curve. Note, however, that there is a wide gap in the data aorund June when the model data collection system was down.

Estimates of the MBE and RMSE for daily and monthly values of UV radiation are presented in Figure 30. In this case the daily MBE and RMSE are 0.35% and 16% while the monthly MBE and RMSE are 0.35% and 4.9%.

6 Discussion

In this section we discuss how our model compares to other similar ones. Moreover we investigate some of the major error sources and try to quantify them. The model has some known shortcomings and suggestions on how to improve and extend future versions are also presented here.

6.1 Comparison with other models

It is well known that the primary source of inaccuracies in surface irradiance models is the effect of clouds, e.g. (Whitlock et al., 1990). Our model is fed with cloud information from MESAN which in turn gets data from SYNOP, the geostationay satellite METEOSAT (every half hour) and the polar orbiting NOAA satellites (about four times a day). These data sources are then weighted together depending on their availability and quality. In Scandinavia the polar orbiting satellites produce data with much better quality than the geostationary satellite which here views the Earth's surface at wide angles.

We compared our model (28% RMSE) with two other models which both use cloud information from geostationary satellites only. The first one is presented in (Olseth and Skartveit, 2001) and is based on a modified version of the Heliosat procedure (Fontoynont et al., 1998). They report an RMSE of 24% for hourly global irradiances. Validation data comes from snow free situations at eight Norwegian and one Swedish station. The horizontal model resolution is ca 10 km which together with the snowfree restriction may explain some of the 4% error difference in favour of their model.

The other model, described in (Perez et al., 1997), is an extension of the pyrheliometer formula given in (Kasten, 1984). Here, the RMSE for modelled hourly global irradiances is said to be 23%, when validated against one station in Albany (42.75° N), USA. Also in this case the horizontal resolution is twice that of our model and the geostationary satellite has a more favourable view angle looking at Albany, which is located closer to the equator than any of the stations in our validation data set.

What about intra- and extrapolating data from the sites in the SMHI radiation network? The distance to the nearest neighbour for the present solar radiation network is between 160–300 km. Interpolation or extrapolation of hourly data over these distances will result in an RMSE of about 35–40% (Perez et al., 1997) so this is not a competitive alternative to the present model. Moreover, this approach limits the covered area and leaves out, for example, most of the Baltic sea. The model error for the hourly global irradiance amounts to 28% which corresponds to the error obtained when extrapolating over a distance of about 50 km. This means that Sweden would have to be covered with 450,000 km^2 / $(\pi\, 50^2)$ km^2 ≈ 60 stations to match the model results. That is five times as many station as in the present network.

6.2 Model error sources

It should be noted that the modelled values will represent an average value for the grid area and not a point estimate. When comparing values of high temporal resolution (hours), the cloud configuration will certainly differ over the grid area. During summer, for example, convective cloudiness with scattered clouds will cause a highly variable radiation field on the subgrid scale.

The model was validated using measurements from the SMHI radiation network. However, the horizontal model resolution is about 20 km which means that each gridpoint represents an area of roughly 400 km^2. The expectation value for the (squared) error made when comparing a model gridpoint value representing the gridpoint average $m = \sum m_i/N$, with a site measurement m_0 can be approximated with

$$\epsilon^2 \;=\; E\left\{(\frac{1}{N}\sum_i m_i - m_0)^2\right\}$$

$$= \frac{1}{N^2}\sum_i\sum_j E\{m_i\, m_j\} + E\{m_0^2\} - \frac{2}{N}\sum_i E\{m_i\, m_0\} \quad (36)$$

where N is the number of subgrid points in the approximation of the grid average. To compute this error we need to know the covariance $E\{m_i\ m_j\}$ between point measurements inside the grid square. The covariance between point measurements is related to their RMSE counterparts ϵ_{ij} according to:

$$\begin{aligned} \epsilon_{ij} &= \sqrt{E\{(m_i - m_j)^2\}}\,/\,E\{m_i\} \quad \Rightarrow \\ E\{m_i\, m_j\} &= E\{m_i^2\} - \frac{1}{2}\,E^2\{m_i\}\,\epsilon_{ij}^2. \end{aligned}$$

Hence, given the expectation value for the squared point irradiance $E\{m_i^2\}$, the squared expectation value of the point irradiance $E^2\{m_i\}$ and the relative RMS errors ϵ_{ij}, we can compute the error in equation (36). Based on relative error measurements for stations in south-eastern New York State and Massachussets (Perez et al., 1997) together with statistics from our own validation data set, we arrived at a relative error $\epsilon/E\{m_0\}$ of about 10% for hourly values of the global irradiance. The grid average was approximated with a sum over $N = 33 \times 33$ subgrid points.

The magnitude of this error source has not been studied for the direct radiation. However, we can at least expect that the error will be larger than for the global radiation since the cloud effect is more pronounced for the direct radiation.

Another factor that especially affects the direct radiation is the lack of information about the aerosols. At present, this information is limited to a climatology. This causes an error which we investigated by comparing modelled irradiances using turbidity from the climatology and turbidity based on measured direct beam irradiances made for clear occasions (without Volcanic influence) at the station in Norrköping. This comparison suggests that the error (hourly values) from using the climatology is around 9% for the direct and 3% for the global irradiance.

In order to validate the instantaneous model output at time t, with the integrated measurements valid for the preceding hour, we made the approximation given by equation (34). The magnitude of this error was estimated by simulating the clear sky global irradiance during a summer day in Norrköping. Hourly instantaneous values were compared to numerically integrated irradiances that mimicked the measurements. The results from this experiment indicate that the RMSE for the global irradiance is almost constant at about 2% throughout the day. In absolute terms this means that the maximum error, due to the time scale differences, is about 20 W/m^2 for the global irradiance in Norrköping.

Leaving out the ground albedo in the cloud effect function is another source of error. The overall effect of this simplification on the estimation and validation procedure has not been studied but it was noted on in section 4.4. It turned out that snow on the ground may alter the cloud effect with as much as 40% which means that this is an issue for future model improvement.

6.3 Future improvements

Even if the model performance was shown to be comparable to that of similar models there are still a number of areas open for model development. Some suggestions on possible future improvements are touched upon below.

A couple of the error sources described in the previous section should for example be considered in the model development procedure. The albedo model should be validated and once this has been done the albedo can be included as a new parameter in the cloud effect function. Once the albedo model is validated it is possible to complement the model with information about the long-wave radiation and the outgoing component which are now the only missing components in the radiation balance.

Another issue in connection with the cloud effect function is that we use the same function for the global and the photosynthetically active irradiance. This was motivated by the fact that the spectral distribution of the PAR lies in the middle of the solar spectrum and the studies showing a high correlation between measurements of global irradiance and PAR (Papaioannou et al., 1993). There are, however, recent work that suggests that there are nonnegligible differences in that the cloud effect is stronger for global radiation than for PAR (Alados et al., 2000). Since we haven't been able to validate the PAR quantity we cannot say how big this difference is but it is clear that finding a suitable validation data set for the PAR is an important issue.

Measurements of the turbidity will soon be available from the 12 stations in the SMHI radiation network. These measurements need to be interpolated to the model grid before they are inserted into the system. Care must be taken when the impact of these measurements is studied since the retrieval of the turbidity is based on the same radiation code that is used for the clear sky calculations.

Increasing the model resolution to about 10 km should be possible if the cloud information is taken directly from the satellites instead as today from the MESAN system, e.g. (Persson, 1997). There is, however, a point in using the MESAN data since our products can then be added to the MESAN system for use together with its other components in a homogeneous and consistent way.

Another problem is that the clear sky model produces zero output when the Sun is under the horizon, or more precisely, when the apparent solar zenith angle is larger than 91°. This means that the irradiance during twilight is neglected which causes problems during the polar night and when the model output is integrated over long time periods. One alternative is to develop a dedicated twilight model and switch to it when and where the Sun has set.

6.4 Applications

We see a number of potential applications that may benefit from the data produced by our model system. The following list covers some areas where people have shown interest in gridded irradiance data.

- Radiation forecasts. Information about the radiative heating and cooling is of interest for indoor climate control. However, new cloud effect functions based on forecasted variables need to be developed.
- UV-index forecasts for public information. More detailed maps could be produced using this model system but a prognostic model version need to be implemented.
- Exposure studies. Since the clear sky model is able to calculate irradiances on tilted surfaces it would be possible to model human exposure to solar irradiance in different situations and locations.

Table 11: Summary of validation results for hourly, daily and monthly values of four of the radiation quantities.

		Global	Direct	Sunshine	CIE UV
Hourly	MBE	-0.28%	1.7%	0.98%	0.21%
	RMSE	28%	53%	53%	29%
Daily	MBE	-0.15%	2.1%	0.92%	0.35%
	RMSE	16%	31%	24%	16%
Monthly	MBE	-0.15%	2.1%	0.92%	0.35%
	RMSE	5.7%	11%	7.3%	4.9%

- Solar energy potential. The possibility to calculate irradiance towards tilted surfaces is also of interest when considering different shapes and constellations of solar cells or solar collectors.
- Mesoscale reanalysis. There is an interest also to include the radiation at the Earth's surface in such a project. This would call for a faster model in order to cope with several decades of hourly data.
- Biological growth models. The photosynthetically active radiation could be useful input in, for example, agricultural and forestry models, or for monitoring of algae blooming in the Baltic sea.
- Radiation balance. In order to be useful for studies of the radiation balance, the model has to be complemented with information about long-wave radiation and the outgoing component.

7 Conclusions

An operational radiation model system has been set up at the Swedish Meteorological and Hydrological Institute. It produces hourly fields of global-, photosynthetically active-, CIE UV- and direct radiation together with sunshine duration at a resolution of about 22×22 km^2 for an area covering Scandinavia and the run off region of the Baltic sea. The model is fed with data from the limited area NWP model HIRLAM, the Baltic sea ice model BOBA and the analysis system MESAN, which synthesise meteorological data from SYNOP, satellites, radar, etc. into gridded fields.

The reason for the development of the model system was a need for gridded fields with information about the spatial distribution of the radiation quantities. Such information allow detailed mappings of the solar radiation climate but is also useful in a wide range of applications dealing with biology and technology affected by solar radiation.

Validation results for all but the PAR quantity are given in Table 11. These errors are of the same order as those reported for similar systems applied to other geographical regions. This result is also comparable to that obtainable with models based solely on SYNOP information. As an example, consider arriving at the same error for the global radiation quantity by measurement extrapolation. In this case one would need a network where the inter-station distances are less than about 50 km. For a region like Sweden this means that a network with some 60 stations would be needed.

Acknowledgement

The authors are indebted to the following organisations for funding the project: the Swedish Environment Agency (Naturvårdsverket), the Swedish Meteorological and Hydrological Institute (Sveriges Meteorologiska och Hydrologiska Institut) and the Swedish Radiation Protection Institute (Statens strålskyddsinstitut).

We also want to acknowledge Lars Häggmark, Karl-Ivar Ivarsson and Per-Olof Olofsson for MESAN, in particular Lars Häggmark for all assistance and patience answering our frequent questions.

The HIRLAM project team is acknowledged for their NWP model HIRLAM, Anders Omstedt and his co-workers are credited for their work on the Bohai and Baltic sea ice model BOBA and the NASA/GSFC TOMS team is acknowledged for making their total ozone data product available in near real time on the Internet.

Finally we gratefully acknowledge Christian Gueymard for the permission to use his radiation transfer model SMARTS2. He has done an excellent work.

Terms and abbreviations

Albedo	Reflected fraction of the perpendicularly incident radiation.
BOBA	Baltic sea ice model.
CIE	International light standardization committee.
Global radiation	Solar radiation on the horizontal plane from the celestial dome.
HIRLAM	High resolution limited area NWP model.
Irradiance	Incident radiation energy per unit time and area. (W/m^2, $J/s/m^2$).
Irradiation	Time integrated irradiance (Wh/m^2, J/m^2).
Long-wave radiation	Radiation of heat from the Earth and the atmosphere, 4–100 μm
MBE	Mean bias error.
MESAN	Mesoscale analysis system.
Mesoscale	Meteorological horizontal scale: a few km up to some hundred km.
NWP	Numerical weather prediction.
PAR	Photosynthetically active radiation, 400–700 nm.
Pyranometer	Instrument measuring the global or diffuse solar radiation.
Pyrheliometer	Instrument measuring the direct solar radiation.
Reflectance	Reflected radiation relative to the incoming.
RMSE	Root mean squared error.
Short-wave radiation	Same as solar radiation.
SMARTS	Simple Model of the Atmospheric Radiative Transfer of Sunshine.
Solar radiation	The radiation emitted by the sun, practically within 290–4000 nm.
Sunshine duration	Time when the direct radiation is above 120 W/m^2.
SYNOP observations	Synoptic (simultaneous and standardized) weather observations.
TOMS	Total ozone mapping spectrometer.
Transmittance	Transmitted radiation relative to the incoming.
UV-A	Ultraviolet radiation, 315–400 nm.
UV-B	Ultraviolet radiation, 280–315 nm.
UV-C	Ultraviolet radiation, 200–280 nm (none at the Earth's surface).

References

Alados, I., Olmo, F. J., Foyo-Moreno, I., and Alados-Arboledas, L. (2000). Estimation of photosynthetically active radiation under cloudy conditions. *Agricultural and forest meteorology*, 102(1):39–50.

Anderson, G. P., Clough, S. A., Kneizys, F. X., Chetwynd, J. H., and Shettle, E. P. (1986). AFGL atmospheric constituent profiles (0–120 km). Technical Report AFGL-TR-86-0110, Air Force Geophysics Lab, Hanscom, AFB, MA.

Ångström, A. K. (1929). On the atmospheric transmission of Sun radiation and on dust in the air. *Geogr. Ann.*, 11:156–166.

Asner, G. (1988). Biophysical and biochemical sources of variability in canopy reflectance. *Remote Sensing of Environment*, 64:234–253.

Asner, G., Wessman, C., Bateson, C., and Privette, J. (2000). Impact of tissue, canopy and landscape factors on reflectance variability of arid ecosystems. *Remote Sensing of Environment*, 74:69–84.

Aurén, T. E. (1939). Radiation Climate in Scandinavian Peninsula. *Arkiv för matematik, astronomi o. fysik*, 26A(20).

Bubier, J., B.N., R., and P.M., C. (1997). Spectral reflectance measurements of boreal wetland and forest mosses. *J. Geophys. Res.*, 102(D24):29483–29494.

CIE (1987). A reference action spectrum for ultraviolet induced erythema in human skin. *CIE Research Notes*, (6):17–22.

CIE (1993). Terminology of photosynthetically active radiation for plants. In *CIE Collection in Photobiology and Photochemistry*, 106/8. CIE.

Clark, R. N., Swayze, G., Gallagher, A., King, T., and Calvin, W. (1993). The u. s. geological survey, digital spectral library: Version 1: 0.2 to 3.0 microns. Technical Report 93-592, http://speclab.cr.usgs.gov, U.S. Geological Survey Open File Report.

Condit, H. R. (1971). The spectral reflectance of american soils. *Photogrammetric Engineering*, 36:955–966.

Coulson, K. and Reynolds, D. (1971). The spectral reflectance of natural surfaces. *J. Appl. Meteor.*, 10:1285–1295.

Davies, J. A., Abdel-Wahab, M., and Howard, J. E. (1985). Cloud transmissivities for Canada. *Monthly Weather Review*, 113:338–348.

Fontoynont, M., Dumortieer, D., Heinemann, D., Hammer, A., Olseth, J. A., Skartveit, A., Ineichen, P., Reise, C., Page, J., Roche, L., Beyer, H. G., and Wald, L. (1998). SATELLIGHT: A www browser which provides high quality daylight and solar radiation data for western and central Europe. In *9th conference on Satellite Meteorology and Oceanography*, pages 25–28, Paris.

Grenfell, T. C., Warren, S. G., and Mullen, P. C. (1994). Reflection of solar radiation by the Antarctic snow surface at ultraviolet, visible and near-infrared wavelengths. *J. Geophys. Res.*, 99(D9):18669–18684.

Gueymard, C. (1995). SMARTS2, A simple model of the atmospheric radiative transfer of sunshine: Algorithms and performance assessment. Technical Report FSEC-PF-270-95, Florida Solar Energy Center.

Gueymard, C. (1998). Turbidity determination from broadband irradiance measurements: A detailed multicoefficient approach. *J. Appl. Meteor.*, 37:414–435.

Haurwitz, B. (1948). Insolation in relation to cloud type. *J. Meteor.*, 5:110–113.

Haykin, S. (1999). *Neural networks : a comprehensive foundation*. Prentice Hall, Upper Saddle River, N.J.

Hummel, J. and Reck, R. (1979). A global surface albedo model. *J. Appl. Meteor.*, 18:239–253.

Häggmark, L., Ivarsson, K.-I., Gollvik, S., and Olofsson, P.-O. (2000). Mesan, an operational mesoscale analysis system. *Tellus*, 52 A:2–20.

ICNIRP (1995). Global solar UV index, A joint recommendation of WHO, WMO, UNEP and ICNIRP. Technical Report ICNIRP-1/95, Intl. Commission of Non-Ionizing Radiation Protection, Oberschleissheim.

Josefsson, W. (1989). Computed global radiation using interpolated, gridded cloudiness from the meso-beta analysis compared to measured global radiation. Meteorologi 101, SMHI.

Josefsson, W. (2000). Measurements of total ozone 1997 - 1999. RMK 91, SMHI.

Josefsson, W. and Landelius, T. (2000). The effect of clouds on uv irradiance: As estimated from cloud amount, cloud type, precipitation, global radiation and sunshine duration. *J. Geophys. Res.*, 105(D4):4927–4935.

Kasten, F. (1984). Parametrisierung der Globalstrahlung durch Bedeckungsgrad und Trübungsfaktor. *Annalen der Meteorologie (Neue Folge)*, 20:49–50.

Kasten, F. and Czeplak, G. (1980). Solar and terrestrial radiation dependence on the amount and type of cloud. *Solar Energy*, 43(34):177–190.

Kylling, A., Albold, A., and Seckmeyer, G. (1997). Transmittance of a cloud is wavelength-dependent in the UV-range: Physical interpretation. *Geophys. Res. Lett.*, 24(4):397–400.

Kylling, A., Stamnes, K., and Tsay, T. S. (1995). A reliable and efficient two-stream algorithm for spherical radiative transfer: Documentation of accuracy in realistic media. *J. Atmos. Chem.*, 21:115–150.

Miller, J., White, H., Chen, J., Peddle, D., McDermid, G., Fournier, R., Shepherd, P., Rubinstein, I., Freemantle, J., Soffer, R., and LeDrew, E. (1997). Seasonal change in understory reflectance of boreal forests and influence on canopy vegetation indices. *J. Geophys. Res.*, 102(D24):29475–29482.

Olseth, J. A. and Skartveit, A. (2001). Solar irradiance, sunshine duration and daylight illuminance derived from METEOSAT data at some European sites. *Submitted to Theor. and Appl. Clim.*

Papaioannou, G., Papanikolauo, N., and Retails, D. (1993). Relationships of photosynthetically active radiation and shortwave irradiance. *Theoretical and Applied Climatology*, 48(1):23–27.

Perez, R., Seals, R., and Zelenka, A. (1997). Comparing satellite remote sensing and ground network measurements for the production of site/time specific irradiance data. *Solar Energy*, 60(2):89–96.

Perovich, D. K. (1996). The optical properties of sea ice. Technical Report 96-1, NTIS, NTIS, Springfield, Virginia 22161, USA.

Persson, T. (1997). Solar irradiance modelling using satellite retrieved cloudiness. RMK 81, SMHI.

Persson, T. (1999). Solar radiation climate in Sweden. *Phys. Chem. Earth (B)*, 24(3):275–279.

Pommeraux, J.-P., Zellner, R., and Pyle, J. (1997). Stratospheric chemistry. In *European research in the Stratosphere*, chapter 4. EC–DGXII, Luxembourg. ISBN 92-827-9719-8.

Shettle, E. P. (1989). Models of aerosols, clouds and precipitation for atmospheric propagation studies. In *Proc. Conf. Atmospheric propagation in the UV, Visible, IR and mm-Wave region and related system aspects*, volume 454, pages 15.1–15.13, Copenhagen, Denmark. AGARD.

SNA (1995). *Klimat, sjöar och vattendrag*. Sveriges nationalatlas. Bra Böcker.

Wallén, C. C. (1966). Global solar radiation and potential evapotranspiration in Sweden. *Tellus*, 18:787–800.

Whitlock, C. H., Staylor, W. F., Darnell, W. L., Chou, M. D., Dedieu, G., Deschamps, P. Y., Ellis, J., Gautier, C., Frouin, R., Pinker, R. T., Laszlo, I., Rossow, W. B., and Tarpley, D. (1990). Comparison of surface radiation budget satellite algorithms for downwelled shortwave irradiance with Wisconsin FIRE/SRB surface-truth data. In *Proc. 7th AMS Conf. on Atmospheric Radiation, San Francisco, CA*, pages 237–242, Boston, MA. American Meteorol. Soc.

WHO (1994). Environmental health criteria no. 160, Ultraviolet radiation. Technical report, World Health Organization, Geneva, Switzerland.

WMO (1986). Revised instruction manual on radiation instruments and measurements. Technical Report WCRP Publ. Series No.7, WMO/TD. No.149, World Meteorological Organization, Geneva, Switzerland.

WMO (1996). Guide to meteorological instruments & methods of observation. Technical Report WMO No. 8, World Meteorological Organization, Geneva, Switzerland.

SMHIs publications

SMHI publishes six report series. Three of these, the R-series, are intended for international readers and are in most cases written in English. For the others the Swedish language is used.

Names of the Series	**Published since**
RMK (Report Meteorology and Climatology)	1974
RH (Report Hydrology)	1990
RO (Report Oceanography)	1986
METEOROLOGI	1985
HYDROLOGI	1985
OCEANOGRAFI	1985

Earlier issues published in serie RMK

1 Thompson, T., Udin, I., and Omstedt, A. (1974)
Sea surface temperatures in waters surrounding Sweden.

2 Bodin, S. (1974)
Development on an unsteady atmospheric boundary layer model.

3 Moen, L. (1975)
A multi-level quasi-geostrophic model for short range weather predictions.

4 Holmström, I. (1976)
Optimization of atmospheric mo dels.

5 Collins, W.G. (1976)
A parameterization model for calculation of vertical fluxes of momentum due to terrain induced gravity waves.

6 Nyberg, A. (1976)
On transport of sulphur over the North Atlantic.

7 Lundqvist, J.-E., and Udin, I. (1977)
Ice accretion on ships with special emphasis on Baltic conditions.

8 Eriksson, B. (1977)
Den dagliga och årliga variationen av temperatur, fuktighet och vindhastighet vid några orter i Sverige.

9 Holmström, I., and Stokes, J. (1978)
Statistical forecasting of sea level changes in the Baltic.

10 Omstedt, A., and Sahlberg, J. (1978)
Some results from a joint Swedish-Finnish sea ice experiment, March, 1977.

11 Haag, T. (1978)
Byggnadsindustrins väderberoende, seminarieuppsats i företagsekonomi, B-nivå.

12 Eriksson, B. (1978)
Vegetationsperioden i Sverige beräknad från temperaturobservationer.

13 Bodin, S. (1979)
En numerisk prognosmodell för det atmosfäriska gränsskiktet, grundad på den turbulenta energiekvationen.

14 Eriksson, B. (1979)
Temperaturfluktuationer under senaste 100 åren.

15 Udin, I., och Mattisson, I. (1979)
Havsis- och snöinformation ur datorbearbetade satellitdata - en modellstudie.

16 Eriksson, B. (1979)
Statistisk analys av nederbördsdata. Del I. Arealnederbörd.

17 Eriksson, B. (1980)
Statistisk analys av nederbördsdata. Del II. Frekvensanalys av månadsnederbörd.

18 Eriksson, B. (1980)
Årsmedelvärden (1931-60) av nederbörd, avdunstning och avrinning.

19 Omstedt, A. (1980)
A sensitivity analysis of steady, free floating ice.

20 Persson, C., och Omstedt, G. (1980)
En modell för beräkning av luftföroreningars spridning och deposition på mesoskala.

21 Jansson, D. (1980)
Studier av temperaturinversioner och vertikal vindskjuvning vid Sundsvall-Härnösands flygplats.

22 Sahlberg, J., and Törnevik, H. (1980)
A study of large scale cooling in the Bay of Bothnia.

23 Ericson, K., and Hårsmar, P.-O. (1980)
Boundary layer measurements at Klock-rike. Oct. 1977.

24 Bringfelt, B. (1980)
A comparison of forest evapotranspiration determined by some independent methods.

25 Bodin, S., and Fredriksson, U. (1980)
Uncertainty in wind forecasting for wind power networks.

26 Eriksson, B. (1980)
Graddagsstatistik för Sverige.

27 Eriksson, B.(1981)
Statistisk analys av nederbördsdata. Del III. 200-åriga nederbördsserier.

28 Eriksson, B. (1981)
Den "potentiella" evapotranspirationen i Sverige.

29 Pershagen, H. (1981)
Maximisnödjup i Sverige (perioden 1905-70).

30 Lönnqvist, O. (1981)
Nederbördsstatistik med praktiska tillämpningar.
(Precipitation statistics with practical applications.)

31 Melgarejo, J.W. (1981)
Similarity theory and resistance laws for the atmospheric boundary layer.

32 Liljas, E. (1981)
Analys av moln och nederbörd genom automatisk klassning av AVHRR-data.

33 Ericson, K. (1982)
Atmospheric boundary layer field experiment in Sweden 1980, GOTEX II, part I.

34 Schoeffler, P. (1982)
Dissipation, dispersion and stability of numerical schemes for advection and diffusion.

35 Undén, P. (1982)
The Swedish Limited Area Model. Part A. Formulation.

36 Bringfelt, B. (1982)
A forest evapotranspiration model using synoptic data.

37 Omstedt, G. (1982)
Spridning av luftförorening från skorsten i konvektiva gränsskikt.

38 Törnevik, H. (1982)
An aerobiological model for operational forecasts of pollen concentration in the air.

39 Eriksson, B. (1982)
Data rörande Sveriges temperaturklimat.

40 Omstedt, G. (1984)
An operational air pollution model using routine meteorological data.

41 Persson, C., and Funkquist, L. (1984)
Local scale plume model for nitrogen oxides. Model description.

42 Gollvik, S. (1984)
Estimation of orographic precipitation by dynamical interpretation of synoptic model data.

43 Lönnqvist, O. (1984)
Congression - A fast regression technique with a great number of functions of all predictors.

44 Laurin, S. (1984)
Population exposure to SO and NO_x from different sources in Stockholm.

45 Svensson, J. (1985)
Remote sensing of atmospheric tempera-ture profiles by TIROS Operational Vertical Sounder.

46 Eriksson, B. (1986)
Nederbörds- och humiditetsklimat i Sverige under vegetationsperioden.

47 Taesler, R. (1986)
Köldperioden av olika längd och förekomst.

48 Wu Zengmao (1986)
Numerical study of lake-land breeze over Lake Vättern, Sweden.

49 Wu Zengmao (1986)
Numerical analysis of initialization procedure in a two-dimensional lake breeze model.

50 Persson, C. (1986)
Local scale plume model for nitrogen oxides. Verification.

51 Melgarejo, J.W. (1986)
An analytical model of the boundary layer above sloping terrain with an application to observations in Antarctica.

52 Bringfelt, B. (1986)
Test of a forest evapotranspiration model.

53 Josefsson, W. (1986)
Solar ultraviolet radiation in Sweden.

54 Dahlström, B. (1986)
Determination of areal precipitation for the Baltic Sea.

55 Persson, C. (SMHI), Rodhe, H. (MISU), De Geer, L.-E. (FOA) (1986)
The Chernobyl accident - A meteorological analysis of how radionucleides reached Sweden.

56 Persson, C., Robertson, L. (SMHI), Grennfelt, P., Kindbom, K., Lövblad, G., och Svanberg, P.-A. (IVL) (1987)
Luftföroreningsepisoden över södra Sverige 2 - 4 februari 1987.

57 Omstedt, G. (1988)
An operational air pollution model.

58 Alexandersson, H., Eriksson, B. (1989)
Climate fluctuations in Sweden 1860 - 1987.

59 Eriksson, B. (1989)
Snödjupsförhållanden i Sverige - Säsongerna 1950/51 - 1979/80.

60 Omstedt, G., Szegö, J. (1990)
Människors exponering för luftföroreningar.

61 Mueller, L., Robertson, L., Andersson, E., Gustafsson, N. (1990)
Meso-γ scale objective analysis of near surface temperature, humidity and wind, and its application in air pollution modelling.

62 Andersson, T., Mattisson, I. (1991)
A field test of thermometer screens.

63 Alexandersson, H., Gollvik, S., Meuller, L. (1991)
An energy balance model for prediction of surface temperatures.

64 Alexandersson, H., Dahlström, B. (1992)
Future climate in the Nordic region - survey and synthesis for the next century.

65 Persson, C., Langner, J., Robertson, L. (1994)
Regional spridningsmodell för Göteborgs och Bohus, Hallands och Älvsborgs län. (A mesoscale air pollution dispersion model for the Swedish west-coast region. In Swedish with captions also in English.)

66 Karlsson, K.-G. (1994)
Satellite-estimated cloudiness from NOAA AVHRR data in the Nordic area during 1993.

67 Karlsson, K-G. (1996)
Cloud classifications with the SCANDIA model.

68 Persson, C., Ullerstig, A. (1996)
Model calculations of dispersion of lindane over Europe. Pilot study with comparisons to measurements around the Baltic Sea and the Kattegat.

69 Langner, J., Persson, C., Robertson, L., and Ullerstig, A. (1996)
Air pollution Assessment Study Using the MATCH Modelling System. Application to sulfur and nitrogen compounds over Sweden 1994.

70 Robertson, L., Langner, J., Engardt, M. (1996)
MATCH - Meso-scale Atmosperic Transport and Chemistry modelling system.

71 Josefsson, W. (1996)
Five years of solar UV-radiation monitoring in Sweden.

72 Persson, C., Ullerstig, A., Robertson, L., Kindbom, K., Sjöberg, K. (1996)
The Swedish Precipitation Chemistry Network. Studies in network design using the MATCH modelling system and statistical methods.

73 Robertson, L. (1996)
Modelling of anthropogenic sulfur deposition to the African and South American continents.

74 Josefsson, W. (1996)
Solar UV-radiation monitoring 1996.

75 Häggmark, L., Ivarsson, K.-I. (SMHI), Olofsson, P.-O. (Militära vädertjänsten). (1997)
MESAN - Mesoskalig analys.

76 Bringfelt, B, Backström, H, Kindell, S, Omstedt, G, Persson, C, Ullerstig, A. (1997)
Calculations of PM-10 concentrations in Swedish cities- Modelling of inhalable particles

77 Gollvik, S. (1997)
The Teleflood project, estimation of precipitation over drainage basins.

78 Persson, C., Ullerstig, A. (1997)
Regional luftmiljöanalys för Västmanlands län baserad på MATCH modell-beräkningar och mätdata - Analys av 1994 års data

79 Josefsson, W., Karlsson, J.-E. (1997)
Measurements of total ozone 1994-1996.

80 Rummukainen, M. (1997)
Methods for statistical downscaling of GCM simulations.

81 Persson, T. (1997)
Solar irradiance modelling using satellite retrieved cloudiness - A pilot study

82 Langner, J., Bergström, R. (SMHI) and Pleijel, K. (IVL) (1998)
European scale modelling of sulfur, oxidized nitrogen and photochemical oxidants. Model development and evaluation for the 1994 growing season.

83 Rummukainen, M., Räisänen, J., Ullerstig, A., Bringfelt, B., Hansson, U., Graham, P., Willén, U. (1998)
RCA - Rossby Centre regional Atmospheric climate model: model description and results from the first multi-year simulation.

84 Räisänen, J., Döscher, R. (1998)
Simulation of present-day climate in Northen Europé in the HadCM2 OAGCM.

85 Räisänen, J., Rummukainen, M., Ullerstig, A., Bringfelt, B., Ulf Hansson, U., Willén, U. (1999)
The First Rossby Centre Regional Climate Scenario - Dynamical Downscaling of CO_2-induced Climate Change in the HadCM2 GCM.

86 Rummukainen, Markku. (1999)
On the Climate Change debate

87 Räisänen, Jouni (2000)
CO_2-induced climate change in northern Europé: comparison of 12 CMIP2 experiments.

88 Engardt, Magnuz (2000)
Sulphur simulations for East Asia using the MATCH model with meteorological data from ECMWF.

89 Persson, Thomas (2000)
Measurements of Solar Radiation in Sweden 1983-1998

90 Daniel B. Michelson, Tage Andersson
Swedish Meteorological and Hydrological Institute (2000)
Jarmo Koistinen, Finnish Meteorological Institute
Christopher G. Collier, Telford Institute of Environmental Systems, University of Salford
Johann Riedl, German Weather Service
Jan Szturc, Instiute of Meteorology and Water Management
Uta Gjertsen, The Norwegian Meteorological Institute
Aage Nielsen, Danish Meteorological Institute
Søren Overgaard, Danish Meteorological Institute
BALTEX Radar Data Centre Products and their Methodologies

91 Josefsson, Weine (2000)
Measurements of total ozone 1997 – 1999

92 Andersson, Tage (2000)
Boundary clear air echos in southern Sweden

93 Andersson, Tage (2000)
Using the Sun to check some weather radar parameters

94 Rummukainen, M.,S. Bergström, E. Källén, L. Moen, J. Rodhe, M. Tjernström (2000)
SWECLIM – The First Three Years

95 Meier, H. E Markus (2001)
The first Rossby Centre regional climate scenario for the Baltic Sea using a 3D coupled ice-ocean model

SMHI
Swedish Meteorological and Hydrological Institute
SE 601 76 Norrköping, Sweden.
Tel +46 11-495 80 00. Fax +46 11-495 80 01

ISSN 0347-2116